Mineralogical, crystallographic, and isotopic constraints on the precipitation of aragonite and calcite at Shiqiang and other hot springs in Yunnan Province, China

Brian Jones[a], Xiaotong Peng[b]

[a] *Department of Earth and Atmospheric Sciences, University of Alberta, Edmonton, T6G 2E3, Canada*

[b] *Institute of Deep-Sea Science and Engineering, Chinese Academy of Science, Sanya, 572000, China*

e-mail address: Brian.Jones@ualberta.ca

Abstract

Two active spring vent pools at Shiqiang (Yunnan Province, China) are characterized by a complex array of precipitates that coat the wall around the pool and the narrow ledges that surround the vent pool. These precipitates include arrays of aragonite crystals, calcite cone-dendrites, red spar calcite, unattached dodecahedral and rhombohedral calcite crystals, and late stage calcite that commonly coats and disguises the earlier formed precipitates. Some of the microbial mats that grow on the ledges around the pools have been partly mineralized by microspheres that are formed of Si and minor amounts of Fe. The calcite and aragonite are interspersed with each other at all scales are both primary precipitates. Some laminae, for example, change laterally from aragonite to calcite over distances of only a few millimeters. The precipitates at Shiqiang are similar to precipitates found in and around the vent pools of other springs found in Yunnan Province, including those at Gongxiaoshe, Zhuyuan, Eryuan, and Jifei. In all cases, the δD_{water} and $\delta^{18}O_{water}$ indicate that the spring water is of meteoric origin. These are thermogene springs with the carrier CO_2 being derived largely from the mantle and reaction of the waters with bedrock. Variations in the $\delta^{13}C_{travertine}$ values indicate that the waters in these springs were mixed, to varying degrees, with cold groundwater and its soil-derived CO_2. Calcite and aragonite precipitation took place once the springs waters had become supersaturated with respect to $CaCO_3$, probably as a result of rapid CO_2 degassing. These precipitates, which were not in isotopic equilibrium with the spring water, are characterized by their unusual crystal morphologies. The precipitation of calcite and aragonite, seemingly together, can probably be attributed to microscale variations in the saturation levels that are, in turn, attributable to microscale variations in the rate of CO_2 degassing.

Keywords: Hot springs, calcite, aragonite, opal-A, isotopes, dendrites

1. Introduction

Thermal springs, found throughout the world (Waring, 1965), are natural laboratories characterized by waters with variable temperatures, pH, and water chemistry. Hot springs with water discharged at temperatures above 37.5°C (Pentecost et al., 2003) to 40°C (Renaut and Jones, 2000) are characterized by bewildering diversity in their mineral assemblages (e.g., calcite, aragonite, opal-A), crystal morphologies (e.g., calcite dendrites), and/or microbiology. As more and more of these hot springs are being examined it is becoming increasingly apparent that they are complex systems controlled by a myriad of intrinsic and extrinsic parameters that may act independently or in unison. The presence of calcite and aragonite, which are common components of many hot spring deposits (Kitano, 1955; Folk, 1974; Renaut and Jones, 1997; Pentecost, 2005), usually engenders the question of what controlled the precipitation of these two polymorphs. As discussed by De Choudens-Sánchez and González (2009, pp. 363-364) the precipitation of calcite as opposed to aragonite, irrespective of where it forms, has been attributed to many different factors such as water temperature, Mg/Ca ratio, and saturation levels. This is certainly true for calcite and aragonite that are commonly found in the deposits around hot springs (e.g., Renaut and Jones, 1997; Peng and Jones, 2013; Jones and Peng, 2014a).

The precipitates in and close to many hot spring vent pools in Yunnan Province, China (Fig. 1), are formed of calcite and/or aragonite and various accessory minerals that commonly develop in association with the microbial mats that thrive in these settings (e.g., Jones and Peng, 2012a; Peng and Jones, 2013; Jones and Peng, 2014b, 2014a). The distribution and crystal morphology of the calcite and aragonite found in these deposits is highly variable at all scales. This is clearly apparent at Shiqiang (also known as Stone Wall) where there are two active but unnamed hot spring pools that are about 3 m apart (Figs. 1, 2). Although both springs have walls

built around them (Fig. 2), the vent pools and their margins remain intact. Samples collected from these springs allow examination of the (1) spatial relationships between the calcite and aragonite, (2) crystal morphologies, (3) modification of the primary precipitates by later precipitates, and (4) preservation of the microbes that reside in and around these springs. These results are then integrated with stable isotope (O and C) data and compared with information derived from other hot springs in Yunnan Province, including those at Eryuan (Jones and Peng, 2012a; Peng and Jones, 2013), Shuzhisti in the Rehai area (Jones and Peng, 2012b), Jefei (Jones and Peng, 2014a), and Gongxioashe and Zhuyuan in the Ruidianxiang area (Jones and Peng, 2014b) (Fig. 1B). This comparison allows assessment of the features that are common to all of the springs across the region and broadens the discussion about the factors that may control the precipitation of the calcite and aragonite within these high temperature environments.

2. General Setting

Sited on the east margin of the Tibet-Yunnan geothermal zone (Kearey and Wei, 1993), Shiqiang sits on the Longchuanjiang Fault (Fig. 1) in the Tengchong volcanic area (Zhang et al., 2008). This part of the Tengchong block, produced by the collision of the Indian and Eurasian plates (Du et al., 2005), experienced considerable faulting and volcanic activity until the early Cenozoic (Zhu and Tong, 1987; Du et al., 2005).

Shiqiang is located at 25° 21’ 40.11” N and 98° 37’ 51.24”, 8 km SSW of Jietou, in a rural part of Yunnan Province where little bedrock exposure exists. There appears to be no information on the bedrock geology of this area. Given that the two springs examined in this study have no formal names, they are herein referred to as S1 and S2 (Figs. 1C, 2). For S1, the spring pool is about 2 m in diameter, surrounded by a ledge that is no more than 50 cm wide, and encircled by boulders that are up to 1 m high. On the pool side of these large boulders,

numerous cobbles and small blocks of rock form a fringe around the spring pool. S2, located about 3 m SW of S1, has a large platform built around it (Fig. 2A). The circular vent pool, ~ 2.5 m in diameter, is surrounded by white tiles that are enclosed by an ornate concrete wall (Fig. 2A).

No climatic information is available specifically for Shiqiang. The climate in this area is, however, very similar to that for Tengchong, which is located 32 km to the SSW (Fig. 1B). Between 1971 and 2000, the subtropical highland climate of the Tengchong area experienced annual rainfall of 1480 mm and annual mean temperature of 14.9°C. The climate is seasonal, with temperatures of 1 to 17°C, rainfall of 73 mm, and 244 hours of sunshine in January, to temperatures of 17 to 24°C, rainfall of 286 mm, and 73 hours of sunshine in June (see Jones and Peng, 2012b, their Fig. 3). The cloud cover associated with the heavy monsoonal rains in June is responsible for the low hours of sunshine during that month.

3. Methodology

Samples of water and precipitates were collected on May 4, 2013. Attempts to collect more samples in 2015 failed because ownership of the land had changed and nobody was allowed onto it. Sampling of the precipitates in and around the pool in 2013 was restricted because it is a tourist site and the owners requested that not leave visible damage from our sampling. A hammer and small chisel was used to obtain small samples from various parts of the deposits. Five small thin sections, each impregnated with blue epoxy to highlight the porosity, were made from these samples in order to establish the large scale fabrics of the precipitates. Small fracture samples (~ 1 cm^3) were extracted from the larger samples for examination on the scanning electron microscope (SEM). After mounting on a SEM stub, each sample was sputter coated with carbon before being examined on a JOEL 6400FE SEM with an

accelerating voltage of 5 kV. Minerals evident in the SEM scans were identified on the basis of their crystal morphology and elemental composition as determined by Energy-dispersive X-ray (EDX) analyses using an accelerating voltage of 20 kV and a Princeton Gamma-Tech X-Ray System that was attached to the SEM. The average spot size for the EDX analyses was ~ 1 μm and analyses were repeated many times in order to verify the presence of the detected elements. A total of 561 SEM photomicrographs along with petrographic analysis of the thin sections allowed detailed assessment of the samples. For some SEM images, the grey levels and contrast were modified using PhotoShop CC ©. For some images, a black background was introduced in order to highlight the main features of the image.

The temperature and pH of the spring waters were measured in the field on May 4, 2013. Water samples, after filtration with a 22 μm syringe membrane, were stored in polypropylene bottles. The cation and anion content of the water samples were determined by the Saskatchewan Research Council (Saskatoon, Canada) within three weeks of collection. The elements Ca, Mg, Na, K, Si and S were measured by Inductively Coupled Plasma Atomic Emission Spectroscopy (ICP-AES); alkalinity (including p alkalinity) was derived by titration with sulphuric acid on an auto-titration system. The bicarbonate, carbonate and hydroxides were calculated from the pH and alkalinity results. The chloride was measured colorimetrically and fluoride was determined by ion selective electrode.

Filtered water samples for $\delta^{18}O_{water}$ and δD_{water} isotope analyses were stored in 5 ml glass vials and analyzed within two weeks of collection. These analyses were undertaken by Isotope Tracer Technologies Inc. (Ontario, Canada). The VSMOW notation is used for reporting the $\delta^{18}O_{water}$ values and the VPDB notation is used for $\delta^{13}C$. For the $\delta^{18}O_{water}$ and δD_{water} analyses, the water was vaporized by a flash process at 140°C and then analyzed using a Picarro Cavity

Ring Down Spectrometer. The reproducibility for the $\delta^{18}O_{water}$ is ±01‰ and for δD_{water} is ±0.6‰. The $\delta^{18}O$ and $\delta^{13}C$ of the calcite and/or aragonite were determined from small samples excavated from various parts of the hand samples by using a needle. Some of these were analyzed by Isotope Tracer Technologies Inc., whereas others were done in the isotope laboratory at the University of Alberta. The reproducibility for the $\delta^{18}O$ and $\delta^{13}C$ is ±0.3‰.

The percentages of calcite and aragonite in the samples used for O and C isotope analyses were determined by X-ray diffraction (XRD) analyses. Each sample, weighing ~ 1 g, was analyzed on a Rigaku Ultima IV Powder XRD system that was run at 38 kV and 38 mA using an Ultima IV X-ray generator with a Co tube. All scans were run from 5° to 90° 2θ at a speed of 2° θ/min. The percentages of calcite and aragonite were determined by using the equation $y = 56.2982x^3 - 1.1170x^2 + 45.2572x$ in which y = % calcite and $x = d_{104}/(d_{104} + d_{111} + d_{021})$ with the d values being the peak heights. This equation, derived by Dr. A. Locock (pers.comm., Electron Microprobe Laboratory, University of Alberta) based on artificial samples created with known percentages of calcite and aragonite, is the same equation as used by Li and Jones (2014). The values obtained by this method are accurate at ±2 wt%. The $\%MgCO_3$ in the calcite was also derived from the XRD analyses by using the equation ($y = -0.334x + 3.037$ where y = the offset of the calcite peak in 2 theta and y = % $MgCO_3$; A. Locock, pers. comm.) derived by Magdans and Gies (2004).

4. Terminology

Herein, a monocrystal is defined as "…a crystalline solid in which the crystal lattice of the entire sample is continuous and unbroken to the edge of the sample with no grain boundaries" (Meldrum and Cölfen, 2008, p. 4336) whereas a mesocrystal (microscopically structured crystal) is constructed of nanocrystals that are "…aligned in a common crystallographic register"

(Meldrum and Cölfen, 2008, p. 4343). Identification of the mesocrystals requires high magnification SEM imaging because XRD analyses cannot reveal the differences between monocrsytals and mesocrystals (e.g., Cölfen and Antonietti, 2005; Meldrum and Cölfen, 2008). Nanocrystals are equivalent to subcrystals as defined by Sandberg (1985), Jones (1989), Jones and Renaut (1996), and Jones et al. (2005) and mesocrystals have been referred to as aggregate crystals (Brinkley et al., 1980; Chafetz et al., 1985; Jones, 1989), composite crystals (Given and Wilkinson, 1985; Sandberg, 1985; Jones and Renaut, 1996), or polycrystalline crystals (Towe and Cifelli, 1967).

Following Jones and Kahle (1986), a dendrite crystal is defined as a crystal with a tree-like morphology with multiple levels of branching.

5. Results

Springs S1 and S2 are both characterized by precipitates that line the wall of the spring vent and are therefore submerged in the hot spring water (Fig. 2C, D). In S2, anthropogenic modifications of the spring mean that only a small part of the precipitates are above water (Fig. 2C). For S1, the situation is different even though the vent pool has been surrounded by small cobbles (Fig. 2E) and a wall formed of boulders (Fig. 2A). Around S1 there is a ledge, typically < 20 cm wide, that is formed of two distinct levels (Fig. 2E, F). The lower ledge is 1 to 2 cm above water level whereas the upper ledge is 3 to 5 cm above water level (Fig. 2E, F). The ledges, covered with a mixture of broken rock fragments and precipitates, are locally coated by green microbial mats (Fig. 2E, F).

5.1. Spring waters

Overall, the compositions of the spring waters from S1 and S2 are very similar to each other (Table 1). The only notable difference is that the water temperature for S1 was 82.5°C

whereas that for S2 was 56.6°C when they were measured on May 4, 2013. Although there is no obvious reason for the temperature difference, there is the possibility that cold groundwater may be mixing with the spring water in S2. Guo and Wang (2012, numbers TCH06 and TCH07 in their Tables 1 and 2) reported water analyses for samples collected in 2009 from two springs that they labelled "Shiqiang I Spring" and "Shiqiang II Spring". Although they noted that these are close to Jietou, they did not provide the precise locations of these springs and it is therefore impossible to know if they are the same two springs that are considered in this study. Relative to the data obtained in this study, the data reported by Guo and Wang (2012) show significantly lower water temperatures and major differences in the water chemistry (Table 1). Given that the precise locations of the samples reported by Guo and Wang (2012) are unknown, their data are not used herein.

Modelling of the waters using PHREEQC Interactive (v3.3.3) and the Water4F database (Parkhurst and Appelo, 1999) indicates that the springs waters from Shiqiang are saturated with respect to goethite, hematite, and talc but undersaturated or slightly saturated with respect to aragonite and calcite (Table 2).

Isotope analyses of water from S1 and S2 yielded values of $\delta^{18}O_{water}$ of -10.97$_{VSMOW}$ ‰ and -10.81$_{VSMOW}$ ‰, respectively, and $\delta^{2}D_{water}$ of -81.5‰ and -81.7‰, respectively.

5.2. General architecture of precipitates

Thin sections made from samples collected from S1 and S2 show they are formed of three main zones (Figs. 3-5) that can generally be traced from the ledge, over the pool margin, and down onto the wall of the spring pool. The distinguishing features of each zone, from the ledge to the pool, are as follows:

- The laminated zone, found mostly on the ledges comprises thin laminae, typically < 1 mm thick, formed of calcite and/or aragonite (Fig. 3A). Although generally flat-lying, small stromatolite-like columns are locally present on the ledge and the lip of the pool (Fig. 3A, B).
- The dendrite zone, found largely on the lip around the spring pool, is herein divided into zones A and B based on the size and general morphology of the dendrite crystals (Fig. 3A–C). The dendrite crystals in zone A are up to 2 mm long and 0.5 mm wide with densely packed branches and little porosity between the branches and between neighbouring dendrites (Fig. 3C). In contrast, the dendrite crystals in zone B are up to 3 mm long and 0.5 mm wide with loosely packed branches and high porosity between the branches and neighbouring dendrites (Fig. 3A, B).
- The spar calcite zone, found largely on the wall of the spring pool, is formed of spar calcite crystals that are irregular in size and shape and generally featureless (Fig. 3A). This zone is cut by circular holes (1-2 mm diameter) that radiate outwards from the basal substrate.

Collectively, the three zones are formed of various combinations of calcite, aragonite, calcite overgrowths on the primary calcite crystals, unattached calcite crystals, and biofilms and filamentous microbes that have been encrusted with microspheres that are formed of Si and lesser amounts of Fe.

The d_{104} peak on the XRD analyses of the calcite samples are typically offset from their normal position, suggesting that they are Mg-calcite rather than pure calcite. Analyses based on the 2Θ offset of this peak, the calcite contains 5 to 8 wt% $MgCO_3$. This value, however, is an average for all the calcite crystals, irrespective or morphology, that are present in each XRD sample. EDX analyses of numerous individual calcite crystals on the SEM, however, showed

that all of the calcite crystals contain Mg, irrespective of their morphology. Although absolute values cannot be derived from the Mg peaks on the EDX analyses, their low intensity suggests that the $MgCO_3$ is low, which is in agreement with the XRD analyses.

5.3. Calcite

The calcite in the samples from springs S1 and S2, which grew from a defined substrate, include (1) individual anhedral to euhedral crystals (Fig. 4D-H), (2) cone-shaped dendrites (Figs. 3D-F, 4C), and (3) spar calcite that is commonly red (Figs. 3A, 4A, B, 5).

5.3.1. Individual calcite crystals

These crystals, typically < 0.1 mm long, are found in the laminated zone where they are commonly arranged side-by-side and thereby collective define micro-lamina (Fig. 3G, 4D, G, H). Although many of these crystals are equant, others are elongate and appear to be the initial stages of a dendrite (Fig. 4D). In many laminae, small bundles of aragonite needles are commonly interspersed around and between the isolated calcite crystals (Fig. 4G, H).

5.3.2. Calcite cone-dendrites

The "dendrite zone" (Fig. 3A-C) includes two zones that are each formed of "cone dendrites" (cf., Jones and Peng, 2014a) that are up to 2 mm high and 0.5 mm in diameter (Figs. 3D-F, 6). Their name reflects the fact that each dendrite has an external shape akin to an ice-cream cone. Each dendrite is formed of branches that arise from the base of the structure and splay outwards with the maximum diameter being determined by the angle at which the branches diverge from the base (Figs. 3D-F, 4). In some crystals, the branches remain close together and the dendrite has a small diameter (Fig. 4D, 6A). In others, the branches splay outwards at high angles to the vertical and the dendrite has a larger diameter (Figs. 3E, 6A, B). The spread of the

branches was controlled by the development of the surrounding crystals as they competed for growth space. Irrespective of their diameter, the cone dendrites have a circular cross-section (Fig. 6C, D) with the top area commonly being characterized by inner and outer rings of crystals (Fig. 6D). Assessing the structure of the individual branches is difficult because (1) crowding of the crystals means that it is difficult to see all sides of a given branch (Fig. 6E-G) and (2) many of the branches have been partly disguised by later calcite overgrowths, the precipitation of other mineral, and/or biofilm coatings. Clusters of aragonite crystals are, for example, commonly found on the top and around the sides of many of the cone dendrites (Fig. 6H). Nevertheless, the branches appear to be formed of calcite rhombs that are up to 50 μm long, 25 μm wide, and 10 μm high. In each branch, these crystals have their long axis inclined towards the center of the cone and relative to the vertical growth axis of the cone dendrite. Each crystal is inset and offset relative to the underlying crystal (Fig. 6E-G).

The density and diameter of the cone dendrites appears to be related to their position within the dendrite zone relative to the spring pool. The part of the dendrite zone furthest away from the spring pool is formed of large-diameter cones that tend to be widely spaced (Fig. 3E). Towards the pool, the dendrites become more crowded and have smaller diameters with relatively little splaying of the branches (Fig. 4D). In the lowest part of the dendrite zone, which is submerged in the pool water, the dendrites are densely packed and commonly appear to be merged, possibly as a result of other calcite being precipitated between the branches (Fig. 4C). These would be equivalent to the “filled-in dendrites” of Buckley (1951, p. 213).

The dendrite zone is characterized by numerous closely-spaced, dark “growth lines” (Fig. 4D, E) that can be traced laterally through neighbouring dendrites, irrespective of their morphology. High resolution images of these branches show that these growth lines are evident

as distinct constrictions that appear to mark the junction between two successive, nested crystals (Fig. 4A, B). These micro-laminations, as defined by the constrictions are, on average, 0.06 mm thick (Fig. 4A).

5.3.3. Spar calcite

The homogeneous spar calcite zone, which faces into the water of the spring pool, is distinctive because of (1) its red to orange colour, and (2) circular tubes, up to 10 mm in diameter, that cut through the zone and open at the surface (Fig. 7). The constituent calcite crystals are tightly interlocking and it is difficult to precisely delineate the morphology of each crystal (Fig. 4A, B). In some areas, however, the crystals appear to have an irregular columnar shape with their long axis sub-perpendicular to the substrate. Lines that cut across neighbouring crystals and highlighted by iron oxide staining are probably growth lines (Fig. 4A). The circular tubes are of unknown origin.

5.4. Aragonite

Aragonite crystals, up to 100 µm long, but typically < 25 µm long and < 10 µm wide, are commonly interspersed among the calcite crystals (Figs. 4E-H, 8A, B). Most crystals are characterized by zig-zag suture lines that are clearly evident on the crystal faces (Fig. 8C) and most have a hexagonal cross-section and either taper to a point or have a truncated terminus (Fig. 8D). These cyclically twinned crystals are identical to those figured by Jones and Renaut (1996, their Fig. 7A-E), Jones and Peng (2014a, their Fig. 4), and Jones and Peng (2014b, their Fig. 6B).

Most of the aragonite laminae are formed of clusters of aragonite crystals that radiate from a common nucleus (Fig. 4E, H). There are, however, scattered examples of aragonite crystals that are arranged in “wheat sheaf” (Fig. 8E) or a “half wheat sheaf” (Fig. 8F). Where present, the wheat sheaves typically have their long axis parallel to bedding.

There is no evidence of any diagenetic alteration to any of the aragonite crystals. There is, for example, no evidence of any hollow aragonite crystals like those documented form spring deposits at Jifei (Jones and Peng, 2014a, their Fig. 6), which is located 135 km ESE of Tengchong (Fig. 1B).

5.5. Spatial relationships between calcite and aragonite

The spatial relationships between the calcite and aragonite is variable at all scales (Figs. 4D-H, 8G-K, 9). At the microscale, this includes (1) individual calcite and aragonite crystals that grow side-by-side from a common substrate (Fig. 4H), (2) aragonite crystals that grow on top of calcite crystals (Fig. 6H), and (3) euhedral calcite crystals that have grown around and encased a bundle of aragonite crystals (Fig. 8G). In the latter case, the boundaries between the calcite and the aragonite needles are sharp and there is no indication that the calcite formed through the alteration of aragonite (Fig. 8G-K). At the macroscale, spatial relationships between the calcite and aragonite includes (1) vertical alternation between calcite and aragonite laminae (Figs. 4D, 8A), and (2) individual laminae where aragonite crystals pass laterally into calcite crystals (Fig. 9A-C). In each situation, there is no evidence that the calcite formed through the alteration of aragonite. In laminae where aragonite gives way laterally to calcite (Fig. 9A), the growth lines that define the laminae are commonly delineated by thin layers of aragonite crystals (Fig. 9D, E). In this situation, the constrictions that highlight the growth lines in the cone dendrites are accentuated by very thin layers of aragonite crystals that are commonly arranged in wheat-sheaf morphology with their long axis parallel to the growth line (Fig. 9E).

5.6. Calcite overgrowths

The surfaces of many primary calcite crystals are partly disguised by secondary calcite overgrowths (Fig. 10). In S2, these overgrowths are formed of cubic mesocrystals, with sides up

to 2 μm long, that are formed of cubic nanocrystals that have sides < 250 μm long (Fig. 10A-C). In S1, the overgrowths involve rhombic mesocrystals that are 1-2 μm long with nanocrystals 250 -500 nm long (Fig. 10D-G). In both springs, these overgrowth crystals commonly merge to form semi-continuous sheets in which the outlines of the constituent mesocrystals are barely perceptible even though the formative nanocrystals are clearly evident (Fig. 10A, H, I).

5.7. Unattached calcite and aragonite crystals

Throughout the samples from S1 and S2 there are numerous "loose" calcite and aragonite crystals that are not attached to a substrate (Fig. 11). These include (1) euhedral dodecahedral calcite crystals up to 25 μm long with 12 pentagonal faces (Fig. 11A-C), (2) euhedral rhombohedral calcite crystals up to 5 μm long that occur singularly or in small clusters (Fig. 11D), (3) euhedral cubic crystals up to 10 μm long (Fig. 11F), and (4) small fans and wheat-sheaves of aragonite crystals (Fig. 11F). Many calcite crystals are characterized by incomplete growth and/or uneven crystal faces (Fig. 11A-C). This is more prevalent with the dodecahedral than the rhombic crystals (Fig. 11). Minute aragonite crystals commonly grew on the surface of the calcite crystals and/or form small bundles that are wedged between the calcite crystals (Fig. 11F). Individual and clusters of unattached calcite crystals are commonly found enmeshed in the microbial mats found in both springs (Fig. 11G-I).

The dodecahedral and rhombic calcite crystals are morphologically similar to crystals that Jones and Peng (2014b, their Figs. 5, 11E) described from Gonhxiasoshe and Zhuyuan hot springs in the Ruidianxiang area (Fig. 1B).

339 *5.8. Microbial mats and opal-A precipitates*

340 At various levels in the deposits from S1 and S2 there are thin, commonly discontinuous
341 laminae formed of biofilms, mineralized filaments, and microspheres (Figs. 12, 13). Many of the
342 biofilms cover substrates that are formed largely of aragonite crystals bundles (Fig. 12A, B).

343 In S1, mineralized filaments, at least 200 μm long with an external diameter of ~ 1 μm, are
344 common features of the microbial mats (Fig. 12A-D). These non-branching filaments, with open
345 lumens 500 to 750 nm in diameter, are encrusted with microspheres up to 500 nm in diameter
346 (Fig. 12C, D). Repeated EDX analyses of the microspheres showed that they are formed largely
347 of Si with subordinate amounts of Fe. The paucity of morphological features means that it is
348 impossible to ally these filaments with any extant taxa.

349 In S2, some biofilms are formed of elongate, bicellular microbes that are up to 15 μm long
350 and 5 μm wide (Fig. 13A, B). They are morphological akin to microbes that Jones and Peng
351 (2014b, their Fig. 9D) illustrated from Gongxiaoshe in Ruidianxiang (Fig. 1B). The microbes
352 are embedded in a biofilm, up to 5 μm thick, that has a smooth surface (Fig. 10C-F). Cross-
353 sections through the biofilm shows that it is typically laminated and contains Si-Fe microspheres
354 (Fig. 13D-F).

355 In many areas, there are concentrations of Si-Fe microspheres that are either randomly
356 dispersed (Fig. 12E) or aligned along thin threads of mucus (Fig. 12F). These microspheres, up
357 to 1 μm in diameter, are solid, pieced by a central hole, or cut by a cleft on one side (Fig. 12G).
358 The spheres with the central hole or cleft are analogous to opal-A spheres documented by Jones
359 and Peng (2014a, their Fig. 12E).

360 In samples from S1 and S2, the Si-Fe microspheres (<250 nm diameter) are commonly
361 associated with thin biofilms that coat bundles of aragonite crystals (Fig. 12H-K). Elsewhere,

the mineralized filaments coated with Si-Fe microspheres are intimately associated with unattached calcite and aragonite crystals (Fig. 12L).

Some of the biofilms include scattered Euglyphida (Fig. 13K) and pennate diatoms (Fig. 13L).

5.9. Oxygen and carbon isotopes

The aragonite and calcite in the samples from S1 and S2 are intercalated at such a fine scale (Figs. 4D-H, 9) that it proved impossible to collect samples for isotope analyses that were purely aragonite or purely calcite. Analyses of 10 micro-samples (each weighing ~ 0.5 μg) taken from various parts of the samples collected from S1 and S2 yielded $\delta^{18}O$ values of -17.8 to -18.8‰ and $\delta^{13}C$ values of +1.8 to 2.9‰. XRD analyses of these samples showed that four of them were formed of pure calcite, five contained < 5 wt% aragonite, and one contained ~30 wt% aragonite.

6. Interpretation of isotopic data

In order to evaluate and place the isotopic data from the two springs at Shiqiang in a meaningful context, these data are evaluated relative to the isotopic data that are available from other springs in Yunnan Province (Fig. 1B, Table 3), including Gongxiaoshe and Zhyuan in the Ruidianxiang area (Jones and Peng, 2014b), Jifei (Jones and Peng, 2014a), Eryuan (Jones and Peng, 2012a; Peng and Jones, 2013), and Shuzhisti (Jones and Peng, 2012b). All of these springs, apart from Shuzhisti, are active hot springs where it was possible to measure the water T and pH, collect water samples for chemical analysis, and collect fresh samples of the precipitates. All samples, apart from those at Jifei came from the vent pool of the spring or ledges around the vent pool. In the case of Jifei, the samples came from precipitates that had formed on a cliff face just below the spring pool (Jones and Peng, 2014a).

6.1. Source of spring water

Zhou et al. (2009, their Fig. 2) demonstrated, based largely on δD_{water} and $\delta^{18}O_{water}$ isotopes, that the thermal waters in China are mostly of meteoric origin and therefore plot on the Global Meteoric Water Line (GMWL) as defined by Craig (1961) and the Chinese Meteoric Water Line (CMWL) as defined by Zheng et al. (1983). Liu et al. (2015) also showed that the springs they studied, including Jifei, plotted on the GMWL, CMWL, and southwest China Meteoric Water Line (SWCMWL). Zhou et al. (2009) argued that differences in the δD_{water} and $\delta^{18}O_{water}$ values from different springs reflected variations due to the effects of latitude and altitude. The δD_{water} and $\delta^{18}O_{water}$ values from the springs considered herein also plot on the GMWL and CNWL and thereby conform with a meteoric origin (Fig. 14).

6.2. Water temperatures based on $\delta^{18}O$

Isotopic equilibrium between the calcite, aragonite, and modern spring water can be assessed by comparing the measured water temperature (MT) and the calculated water temperature derived from the $\delta^{18}O$ of the calcite and/or aragonite. Application of the equations developed by Anderson and Arthur (1983), Hays and Grossman (1991), Kim and O'Neil (1997), O'Neil et al. (1969), and Chacko and Deines (2008), however, give different calculated temperature values (CT-I) over a range of ~ 7°C (Fig. 15). Coplen (2007), based on samples from Devils Hole, Nevada, argued that many of the commonly used equations for calculating T from $\delta^{18}O$ produce values that are 8°C too low and therefore proposed a new equation for this purpose. Kele et al. (2015), using travertine and tufa samples collected close to the spring vents in order to avoid downslope changes due to evaporation and degassing, also developed a new equation for deriving T. They argued that it should produce more realistic temperatures because it is based on natural samples collected over a T range of 6 to 95°C. Application of all these equations to samples collected from various springs in Yunnan Provinces showed that the values derived from the equations developed by Coplen (2007) and Kele et al. (2015) consistently produced calculated water temperature (CT-II) values that are 5 to 10°C higher than those derived from the other equations (Fig. 15).

Comparison of the MT with the CT-I values, shows that for five of the six springs, the MT values exceeds the CT-I by up to 28°C (Fig. 15). The only exception is for Shiqiang-S2 where the MT falls within the range of CT-I values (Fig. 15). If the CT-II values are included in the comparison, then only three of six springs have MT that exceed the calculated T (Fig. 15). Among these springs, one is only a few degrees above the CT–II values whereas the other two have MT that are 11-21°C above the highest calculated T (Fig. 15). The discrepancies between

the MT and the calculated temperatures may be partly or entirely due to any of the following reasons:

- Although minerals are being precipitated from the modern springs, the age of the oldest precipitate is unknown. Thus, there is no guarantee that all of the precipitates formed from waters that have the same composition as today. Liu et al. (2015), based on available records, suggested that the hydrochemistry of the hot springs at Jifei had remained constant for at least the last 30 years. Although it is difficult to evaluate the other springs because of the lack of long term records, available information suggests that many of these springs have been relatively stable in terms of their temperature and pH for decades. In addition, the deposits themselves are relatively consistent in nature and generally lack any indications of major changes in the nature of the spring water. At Jifei, isotope values derived from calcite that had precipitated inside a PVC pipe over a 6 month period prior to collection on May 4, 2013 yielded $\delta^{18}O_{calcite}$ and $\delta^{13}C_{calcite}$ values similar to those derived from the calcite and aragonite that had formed close to a nearby spring (see Jones and Peng, 2014a, their Table 4). Albeit with caution, it seems reasonable to assume that the spring deposits considered herein probably formed under isotopically similar conditions to the modern spring water.
- Many samples used for the isotope analyses may be formed of both calcite and aragonite because it was impossible to physically separate the two minerals that are intermixed at the microscale (Figs. 4D-H, 9). This situation is further complicated because it is impossible to obtain thin sections, SEM, XRD, and isotopic analyses from exactly the same sample. Thus, in some cases, XRD analyses showed that a sample was formed entirely of calcite whereas thin section and SEM petrography of samples taken from the same part of the

precipitates clearly show that aragonite is present. For some samples, the problem reflects scale, as the amount of aragonite present may be too small for detection by XRD analysis. In other cases, however, the variance simply reflects the fact that different samples, even though closely spaced, are mineralogically different because of the microscale variance in composition.

Although the same problem existed with the calcite-aragonite deposits at Jifei, Jones and Peng (2014a, their Table 4) showed that there was no obvious correlation between the $\delta^{18}O$ of the sample and the percentage of calcite in the sample (Table 3; Fig. 16). Similarly, Kele et al. (2015, their Fig. 5A) found no obvious correlation between the percentage of calcite and the $\delta^{18}O$ of various samples that had been collected from many different springs in Europe. This is the same with the samples from Shiqiang (Table 3, Fig. 16). The problem of mixed calcite-aragonite samples can, to some extent, be overcome by using two CT values for each sample – one based on the assumption that the sample is 100% calcite and one based on the assumption that it is 100% aragonite. For the Chinese spring samples, the CT values derived for 100% calcite and 100% aragonite using the equations provided by Chacko and Deines (2008) produced a variance of ~ 9 to 10°C for each sample (Fig. 15). This range of CT values always encompasses the CT-I values but not the CT-II values (Fig. 15).

- As noted by Beck et al. (2005), Zeebe (2007), and Kele et al. (2015), there is the potential that the $\delta^{18}O$ of precipitates may be related to the pH of the parent water. With this scenario, the $\delta^{18}O$ of precipitates will decrease in accord with the change in the dominant DIC, which is CO_2 (aq) at pH<6, CO_3^- between pH of 6 and 9.5, and CO_3^{2-} when pH>10 (Zeebe, 2007; Hill et al., 2014). Kele et al. (2015), however, noted that it is difficult to

determine if this is applicable in hot spring systems because it is hard to isolate the changes due to pH as opposed to other parameters such as T, degassing rates, and ionic strength. Kele et al. (2015, p. 187) were, for example, unable to demonstrate any relationship between pH and any other parameter of the spring deposits. In the case of the Chinese springs considered in this study, the pH of the parent water ranges from 6.7 to 8.5 and therefore fall in the range where CO_3^- is the dominant DIC. The potential impact on the $\delta^{18}O$ of the precipitates that form from these waters should, therefore, be negligible.

Comparison of the CT with MT for the springs at Shiqiang, Gongxiaoshe, Zhuyuan, Jifei, and Eryuan (Fig. 15), indicates that the $CaCO_3$ precipitated in those springs is not in equilibrium with the O isotopes of the modern spring waters. The fact that there is no correlation between % calcite and $\delta^{18}O$ values in the Chinese samples (Fig. 16) supports this notion.

6.3. Comparison of $\delta^{18}O_{VSMOW}$ and $\delta^{13}C_{VPDB}$

A cross-plot of $\delta^{18}O_{VSMOW}$ versus $\delta^{13}C_{VPDB}$ shows that the isotopic signatures from the Shiqiang spring deposits are similar to those from Jifei and Eryuan but different from those derived from the spring deposits at Gongxiashe and Zhuyuan at Ruidianxiang and Shuzhishi (Fig. 17). These comparisons must be treated with some caution because the samples from Shiqiang, Jifei, Eryuan, Zhuyuan, and Gongxiaoshe are, as noted above, formed of mixed calcite and aragonite. In the Eryuan spring deposits, amorphous calcium carbonate (ACC) is also present with the calcite and aragonite (Jones and Peng, 2012a). In contrast, the deposits at Shuzhishi are formed entirely of calcite. This situation can be compared to precipitates found around springs at Chemurkeu, which are located on the west shore of Lake Bogoria in the Kenyan Rift Valley (Renaut and Jones, 1997, their Figs. 1, 2). Like the Chinese springs, those

deposits are formed of intercalated calcite and aragonite (Renaut and Jones, 1997, their Fig. 3, 6, 7). In the Kenyan samples, however, the aragonite and calcite crystals are large and isotopic values can easily be determined for each polymorph (Fig. 17). This shows that the aragonite and calcite values are characterized by slightly different values but with both sets being significantly different from the values derived from the Chinese springs (Fig. 17).

The $\delta^{13}C$ signatures of spring deposits have been used to divide them into meteogene (0 to –11‰ with an average of –7‰, Pentecost, 2005, his Fig. 46a) and thermogene (–3 to +8‰ with an average of +3.89‰, Pentecost, 2005, his Fig. 46c) travertines, which reflect the origin of the carrier CO_2 (Pentecost and Viles, 1994; Pentecost, 2005). The $\delta^{13}C$ values for the Chinese spring precipitates fall between these end members, with those from Shiqiang (S1 and S2), Eryuan, and Jifei having $\delta^{13}C_{CaCO_3}$ values between +1 and +3‰, whereas the samples from Zhuyuan, Gongxiaoshe, and Shuzhishi having values between –0.5 and –3.1‰ (Fig. 17). Some of the Chinese $\delta^{13}C_{CaCO_3}$ and $\delta^{18}O_{CaCO_3}$ values are comparable with the values that Kele et al. (2008, their Fig. 13) compiled from various Hungarian springs (Fig. 18). Precipitates from the springs at Shiqiang, for example, plot within the same field as the spring deposits from Egerszálok (Hungary), whereas those from Eryuan and Jifei partly overlap those from Egerszálok (Fig. 18). In contrast, the $\delta^{13}C_{CaCO_3}$ and $\delta^{18}O_{CaCO_3}$ values from Zhuyuan, Gongxiaoshe, and Shuzshishi are different from any of the Hungarian springs, largely because their $\delta^{18}O_{CaCO_3}$ values are significantly lower (Fig. 18). The $\delta^{13}C_{CaCO_3}$ and $\delta^{18}O_{CaCO_3}$ values from the Kenyan precipitates are close to those from Hungary but differ significantly from the Chinese spring values (Fig. 18). Kele et al. (2008) argued that the deposits from Egerszálok fall between the thermometeogene to thermogene travertine as defined by Pentecost (2005). The precipitates from Shiqiang, Eryuan, and Jifei fall in the transition zone that exists between the meteogene and

theremogene travertines. Based on the $\delta^{13}C_{CaCO_3}$ and $\delta^{18}O_{CaCO_3}$ values, Kele et al. (2008) argued that the travertine at Egerszálok formed by rapid precipitation from meteoric water that had experienced deep circulation. Pentecost (2005) argued that the $\delta^{13}C$ in thermogene springs reflects the combined effects of water-rock reactions, rapid CO_2 degassing, and possibly a magmatic CO_2 component.

6.4. Source of CO_2

Potentially, the source of the CO_2 can be assessed from the $\delta^{13}C_{CaCO_3}$ values, providing the $\delta^{13}C_{CaCO_3}$ values are derived from samples close to the spring orifice where secondary modifications of the isotopic carrier, including those caused degassing, are minimized (Kele et al., 2011). Panichi and Tongiorgi (1976), used data from 11 springs in Italy to link $\delta^{13}C_{CO_2}$ to $\delta^{13}C_{CaCO_3}$ by the equation $\delta^{13}C = 1.2\ (\delta^{13}C_{CaCO_3}) - 10.5$. Application of that equation to the Chinese springs yielded $\delta^{13}C_{CO_2}$ values that vary from –13.98‰ at Shuzhisti to –7.9‰ at Shiqiang–S1 (Table 4). Emrich et al. (1970, their Fig. 1) determined the C isotope fractionation factor based on experiments over the range of 20 to 60°C, which is generally lower than the water T associated with the Chinese springs considered herein. Albeit with caution, use of fractionation factors extrapolated from their graphical plots (Emrich et al., 1970, their Fig. 1) yielded $\delta^{13}C_{CO_2}$ values of –4.6 to –9.9‰ (Table 4). Romanek et al. (1992) also determined the C fractionation factor between 20 to 40°C, which is also generally below the temperatures of the Chinese hot springs examined in this study. Nevertheless, extrapolation of their equation produced $\delta^{13}C_{CO_2}$ values of +0.5 to –9.9‰ (Table 4). Chacko et al. (1991), based on experimental data and theoretical considerations, derived the C fractionation factor over a wide range of temperatures and revised the values previously derived by application of the equation

proposed by Bottinga (1968). Application of the equation developed by Chacko et al. (2001, their Appendix 2, top of p. 76), produced $\delta^{13}C_{CO_2}$ values of –2.9 to –8.2‰ for the Chinese spring deposits (Table 4). Derivation of the $\delta^{13}C_{CO_2}$ values from the Chinese spring data using these four approaches, however, produces a diffuse array of results (Table 4). Herein, the equation proposed by Panichi and Tongiorgi (1976) is not used because, as noted by Rimondi et al. (2016), their equation was (1) based on precipitates that formed in surface environments where rapid degassing would have strongly affected the $\delta^{13}C_{CO_2}$ that they measured from the CO_2 gases, and (2) ignores the relationship that exists between temperature and C fractionation. Rimondi et al. (2016), in analyzing their data, found that the equation of Panichi and Tongiorgi (1976) produced $\delta^{13}C_{CO_2}$ values that were far more negative than those generated from the equation proposed by Bottinga (1968). The same is true for the Chinese springs considered herein. The schemes embedded in Emrich et al. (1970) and Romanek et al. (1992) are not used because extrapolation is needed to extend their low temperature experimental data into the higher water temperatures of the Chinese hot springs. Accordingly, the $\delta^{13}C_{CO_2}$ values using the equations developed by Chacko et al. (1991) are used because their fractionation values, which take temperature into account, are based on experimental data and rigorous theoretical calculations.

The $\delta^{13}C_{CO_2}$ values derived for the springs at Shiqiang, Eryuan, Gongxiaoshe, Zhuyuan, and Shuzhisti, ranging from –3.1 to –8.2‰, are comparable to values obtained from 11 springs (–1.1 to –6.4‰) in Yellowstone National Park (Craig, 1953), 55 springs (0 to –7‰) on North Island, New Zealand (Hulston and McCabe, 1962), and –3.2‰ for Pamukkale, Turkey (Kele et al., 2011). Panichi and Tongiorgi (1976), based on 110 samples from cold and thermal springs,

fumaroles, and mofettes in southern Italy obtained $\delta^{13}C_{CO_2}$ values ranging from +1.8 to –21.3‰ with an average value of –2.8‰.

Consideration of all of the available information suggests that the Chinese spring waters, which are of meteoric origin, were heated at depth but probably underwent some modification as they rose to the surface, possibly by mixing with shallower, colder groundwater. That different degrees of mixing were involved is reflected by the variability in the $\delta^{13}C_{CaCO_3}$ values (Fig. 17). At Jifei, for example, Liu et al. (2015) argued that the meteoric water is heated at a depth of ~ 1792 m and ascends along the Kejiehe Fault and Apianzhai Fault where it is mixed with cold groundwater before issuing from the spring vents. Based on the silica-enthalpy method, they suggested that ~44% of the spring water was derived from shallow, cold groundwater.

Around Tengchong, the CO_2 that commonly forms >90% of the total gases associated with the hot springs may have come from the mantle (Liao et al., 1991; Shangguan et al., 2000; Ren et al., 2005; Shangguan et al., 2005; Du et al., 2006; Cheng et al., 2014). The amount of CO_2, however, varies with time. At Dagunguo, which is close to Shizhisti in the Rehai geothermal area, the percentage of CO_2 in the gases ranged from 49.7% in 1980 to 35.3% in 1990 to 97.4% in 1998 to 99.7% in 2000 (Du et al., 2005, their Table 4). These variations have been attributed to (1) earthquake activity (Ren et al., 2005), (2) hydrothermal explosions (Shangguan et al., 2005), and/or (3) temporal changes in the relative contributions from the mantle, crust, and atmosphere (Du et al., 2005).

High $\delta^{13}C_{CaCO_3}$ values have also been found in springs deposits at Dawanzhangjiagou, which is located ~175 km north of Chengdu (Shi et al., 2014) and ~ 965 km NE of Tengchong. Although Shi et al. (2014) did not use the classification of Pentecost and Viles (1994), they argued that the high $\delta^{13}C_{CaCO_3}$ indicated that (1) the decarbonation reaction resulted from deep

thermal metamorphism, and (2) much of the CO_2 came to the surface along the faults and fractures that cut through the bedrock in that area. Their $\delta^{13}C_{CaCO_3}$ values ranged from +3.6 to +9.1‰ (Shi et al., 2014, their Fig. 4), with an average of +5.6‰. Zhou et al. (2015) argued that CO_2 emissions associated with hot springs in the western Sichuan Province increased significantly following major earthquakes such as the Wenchuan Ms 8.0 earthquake that occurred on May 12, 2008. They also noted that following the earthquake, the mantle contribution to the hot springs gradually decreased while the CO_2 and CH_4 derived from organic matter increased. Critically, their data show that the CO_2 content of spring waters varies with time.

7. Discussion

The two springs at Shiqiang are characterized by an array of precipitates with distinctive crystal forms that are similar to those associated with many other hot springs in Yunnan Province (Fig. 1B). This provides an opportunity for determining the commonalities among the precipitates to see if (1) they can provide insights into the factors that control precipitation of the different components found in these settings, and (2) they have the potential of becoming the hallmark of such deposits. Accordingly, the two active hot springs at Shiqiang, documented herein, are compared with (1) Gongxiaoshe and Zhuyuan in the Ruidianxiang area (Jones and Peng, 2014b), (2) Eryuan (Jones and Peng, 2012a, 2014b), (3) Jifei (Jones and Peng, 2014a), and (4) Shuzhishi in the Rehai Geothermal area (Jones and Peng, 2012b). All of these deposits formed from waters that had a temperature of 56 to 88°C and pH of 6.7 to 8.5 (Table 2). Comparisons of the precipitates from all of these springs allows an assessment of their mineralogical, crystallographic, and isotopic features that can be considered diagnostic of

deposits in and around hot spring vent pools in Yunnan (Table 5). In this context, the following points are critical:

- All of the deposits, except for those at Shuzhishi, are formed of calcite and lesser amounts of aragonite (Table 3). At Shuzhisti, no aragonite is present.
- The calcite in these deposits is dominated by dendrite crystals of various sizes and morphological complexity. The crystals vary from the simple cone-dendrites found in Jifei and Shiqiang (Figs. 3D, E, 6) to the geometrically complex calcite bushes at Shuzhishi (Jones and Peng, 2012b, their Figs. 4, 5).
- All of the aragonite crystals are characterized by their (1) hexagonal cross-sectional shape (Fig. 8D), (2) pointed or square terminations (Fig. 8B, D), and (3) complex cyclical twinning with zig-zag suture lines being apparent along the length of their crystal faces (Fig. 8C; Jones and Renaut, 1996, their Fig. 7A-E). Such twinning is apparent on crystals that occur individually, in radiating bundles, or in wheat-sheaves.
- The spatial relationships between the calcite and aragonite is variable in all deposits. This is amply demonstrated in the Shiqiang deposits where the spatial relationships include (1) aragonite that grew on the top and sides of the calcite dendrites (Fig. 4H), (2) interspersed aragonite and calcite crystals rooted on the same substrate (Fig. 6A, B), (3) bundles of aragonite crystals encased by a single euhedral calcite crystal (Fig. 6G-K), (4) aragonite bundles that form thin laminae that interrupted growth of the calcite dendrites (Fig. 4D, E), and (5) individual laminae that grade, over a short distance, from aragonite crystals at one end to calcite crystals at the other end (Fig. 4A).
- The lack of evidence indicating that the aragonite is being diagenetically altered to calcite. For example, where aragonite crystals are encased by calcite, the boundaries between the

aragonite crystals and the encasing calcite are sharply defined with no evidence of modification (Fig. 6H, K). Greer et al. (2015) illustrated aragonite and calcite crystals from a travertine sample collected from the edge of an artificial pond at Shiqiang (precise location not specified) that are morphologically akin to the aragonite crystals and dodecahedral calcite crystals illustrated herein. Their SEM images, for example, included aragonite crystals with zig-zag suture lines (Greer et al., 2015, their Fig. 7b) and calcite crystals growing around bundles of aragonite crystals (Greer et al., 2015, their Fig. 4d–f). Using this information, Greer et al. (2015) argued that the aragonite formed through transformation of the calcite with the nucleation of the aragonite taking place inside the calcite crystals. This model of aragonite formation, however, is not supported by the petrographic relationships evident in their illustrations and documented herein. Specifically, there is no petrographic evidence to support the notion that the aragonite formed by recrystallization of the calcite.

- The paucity of evidence of aragonite or calcite dissolution. Apart from some aragonite crystals at Jefei with leached cores (Jones and Peng, 2014a, their Fig. 6) and some calcite crystals in the Shuzhishi deposits with partly etched surfaces (Jones and Peng, 2012b, their Fig. 8), evidence of dissolution is lacking.
- Secondary calcite overgrowths are evident on calcite crystals found at Shiqiang (Fig. 10) and Shuzhishi (Jones and Peng, 2012b, their Fig. 9). Where present, the overgrowths disguise the morphology of the original calcite crystals.
- Common to all of the spring deposits are unattached euhedral dodecahedral and rhombohedral calcite crystals that commonly display incomplete crystal faces and edges (Fig. 11, 12). These crystals were probably liberated from microbial mats (Fig. 11G, H).

- Microbes and biofilms are present in all of the deposits. Most biofilms are not mineralized and the probability of them being preserved in older deposits is low. Exceptions occurs where silicification has preserved some of the biofilms and their formative microbes, as at Shiqiang (Figs. 12, 13).
- Si-Mg reticulate coatings (cf., Jones and Peng, 2014b, their Fig. 7) are present in some deposits but not others (Table 5). Until the origin of these coatings is resolved (see Jones and Peng, 2014b, pp. 80-83) it is impossible to explain the distribution pattern of this distinctive precipitate that commonly coats the calcite and aragonite crystals.
- In some deposits there are small quantities of accessory diagenetic minerals (Table 5) that probably formed by evaporation of fluids that permeated through the calcite and/or aragonite crystal precipitates and/or formed in association with biofilms (Jones and Peng, 2014a).

The intimate association of calcite and aragonite in spring deposits has been debated even since Meigen (1901) first argued that temperature (T) was the main control with aragonite being precipitated from high temperature waters. Suganuma (1928), however, argued that this was not always the case in Japanese hot springs because aragonite was precipitated in alkaline systems irrespective of temperature whereas calcite was always precipitated in the presence of free carbonic acid. Subsequent attempts to identify the underlying cause of the precipitation of these two polymorphs has involved many different approaches. Folk (1994, his Fig. 2) and Pentecost (2005, his Fig. 37), for example, plotted the occurrences of calcite and/or aragonite in various spring deposits against the T, Mg/Ca ratio, and/or the Mg content of the spring water. Such plots led Folk (1994) to argue that (1) aragonite forms if T > 40-45°C, regardless of water composition, (2) aragonite forms if the Mg/Ca ratio is > 1, regardless of water T, and (3) calcite

forms from water that is Ca-rich and < 40°C. Although generally applicable, Folk (1994) noted exceptions in springs with excessive CO_2 degassing or the slow movement of ions if viscous fluids or mucus films were present. Pentecost (2005), based on plots similar to those of Folk (1994) and various laboratory results, also argued that aragonite and calcite were precipitated from hot water (30 to 60°C) with aragonite only being precipitated at lower T if there were high concentrations of Mg. He also suggested that either calcite or aragonite could be precipitated if the temperature was between 30 and 40°C. In many spring systems these general principles seem applicable. At Mammoth hot springs, for example, Fouke et al. (2000) showed that aragonite formed where water T > 44°C, calcite and aragonite formed where water T was 30 to 43°C, and only calcite formed if the water T was < 30°C. Based on experiments, Kitano (1955) suggested that aragonite formed from water with a T >50°C, but later noted that other experiments showed that this was not always the case (Kitano, 1962a). Kitano et al. (1962) also argued that in spring waters with the same chemical constituents, pH, and T, the proportion of aragonite increased relative to calcite as the rate of CO_2 gas increased. Guo and Riding (1992) argued that the alternating laminae of aragonite and calcite feather crystals in the Rapolano Term deposits of Italy may reflect a variety of different processes. Although noting that the aragonite precipitation may be related to temperature or saturation levels, they suggested that the close associated between the aragonite and organic nuclei might point to an organic origin. In contrast, the argued that the feather calcite crystals resulted from abiotic processes. Okumura et al. (2013), argued that precipitation of the thinly laminated calcite/aragonite deposits found in the Myoken hot spring (Japan), reflected diurnal precipitation cycles that were, to a large extent, mediated by microbes and biofilms.

Arguments like these indicate that the factors that control calcite versus aragonite precipitation are complex and influenced by many different parameters. de Choudens-Sánchez and González (2009, pp. 363-364), based on an exhaustive literature review of calcite and aragonite precipitation worldwide, showed that aragonite as opposed to calcite precipitation has been attributed to numerous variables including T, Mg or Mg/Ca ratio, presence of anions such as PO_4 and SO_4, organic compounds and acids, CO_2 controlled kinetics, and many other factors. They argued, however, that T, the Mg/Ca ratio, and/or CO_2-controlled kinetics were the main controlling factors. In this respect, one of the most notably features of the water chemistry of the Chinese springs is the Mg content that is typically lower than the Ca content (Table 1). At Shiqiang, for example, the Mg:Ca ratio of 0.35 (ratio based on ppm) or 0.63 (molar ratio) for the spring water is essentially the same for both springs. The only exception to this is one sample collected from Gongxiaoshe that has a Mg content slightly higher than that of Ca (Table 1). According to Folk (1994, his Fig. 2), the Mg:Ca ratios for the Shiqiang springs should lead to the precipitation of calcite T is < 40°C, mixed aragonite and calcite between 40 and 60°C, and aragonite when T is > 60°C. In S2, however, where the water T is 82.6°C, the samples are formed largely of calcite (Table 3). In S1, where the water T is 52.6°C, the samples are formed of various admixtures of calcite and aragonite (Table 3). When considered together it is evident that there is no relationship between the Mg:Ca ratio and the polymorph that forms most of the samples.

Many assumptions are inherent to the field- and laboratory-based approaches to deciphering the parameters that control aragonite and calcite precipitation in hot spring systems. The field-based approach used by Folk (1994) and Pentecost (2005), for example, tacitly assumes that the precipitates formed from waters like the modern spring waters that were used to

determine the T, pH, and chemical constituents. Similarly, experimental approaches have typically restricted the number of variables involved and used abiotic systems. Irrespective of the investigative approach used, all have assumed that scale is not critical with the precipitation of one polymorph or another being directly linked to a specific characteristic of the parent water such as T or the Mg:Ca ratio. Analyses of the precipitates from Shiqiang clearly demonstrate that the spatial relationships between the aragonite and calcite are highly complex at all scales. This is also evident in the precipitates from Eryuan (Peng and Jones, 2013), Gongxiaoshe and Zhuyuan (Jones and Peng, 2014b), and Jifei (Jones and Peng, 2014a).

In S1 and to a lesser extent in S2 at Shiqiang, there is a distinct ledge around the spring pool such that the precipitates can be divided laterally into those that are in direct contact with the spring water and those that are slightly elevated above water level (Fig. 2E, F). The green microbial mats (Fig. 2E, F) that grow on the exposed ledges probably develop in a temperature regime that is cooler than that of the spring water. This assessment is supported by the presence of a diverse microbiota that includes euglyphida and some diatoms, which are known to require temperatures of < 45°C (Owen et al., 2008). The mats on the ledges, which commonly cover calcite crystals and bundles of aragonite crystals (Fig. 12A, B, H, L), are characterized by Si-Fe microspheres that encrust the filamentous microbes (Fig. 12C, D) or are embedded in the biofilm (Fig. 13A-F). The Si-Fe precipitates are not found anywhere else in the spring system. In a parallel situation in the Loburu hot springs in the Kenyan Rift Valley, Renaut et al. (1998, p. 1083) attributed silicification of microbial mats to the "…evaporative concentration and rapid cooling of spring waters that had been drawn upward through the mats and microstromatolites by capillary processes." Such an explanation appears equally as valid for the Shiqiang springs.

The presence of microbial mats on the ledges around the spring pools at Shiqiang, which clearly grew under temperature conditions lower than in the spring pool, raises the possibility that the distribution of the calcite and aragonite may be related to temperature variations. This scenario, however, is discounted because the red spar calcite (Fig. 7) is submerged in the spring water (82.5°C in S1) whereas most of the aragonite tends to found in the thinly laminated, interior part of the sample that probably formed on the ledges where the precipitates developed in lower temperature conditions given that they were not in direct contact with the spring water. Such an arrangement is contradictory to the scenario predicted by models such as those proposed by Kitano (1962a, 1962b), Folk (1994), and Pentecost (2005). Similar arguments can also be developed for the spring deposits found at Eryuan, Gongxiaoshe, Zhuyuan, and Jefei.

Evident from the samples from Shiqiang and other springs in the Yunnan Province is that the various $CaCO_3$ polymorphs commonly develop in very close proximity to each other. At Eryuan, for example, ACC, aragonite, and calcite commonly form within microns of each other (Peng and Jones, 2013). There, the different polymorphs form within biofilms where subtle differences in the physical and chemical properties of neighbouring microdomains in the hydrogels of the biofilm probably control the precipitation of the different polymorphs. Although the unattached dodecahedral and rhombic calcite crystals in the Shiqiang deposits probably grew in a biofilm, there is no direct evidence that the biofilms played any role in the precipitation of the primary aragonite and calcite crystals.

Any factor(s) invoked to explain precipitation in and around the vent pools of hot springs in Yunnan province must allow for the precipitation of the various $CaCO_3$ polymorphs, the growth of the complex calcite dendrites, and the precipitation of the accessory minerals. The growth of dendrite crystals is commonly related to very high levels of saturation with respect to $CaCO_3$.

Given that it is usually impossible to determine the exact factors that drive the system to supersaturation, Jones and Renaut (1995, their Fig. 14) related crystal morphologies to a "disequilibrium factor", which included all of the parameters (e.g., CO_2 degassing) that caused the spring water to become supersaturated with respect to $CaCO_3$. According to their scheme, dendrites developed under relatively high levels of supersaturation. Oaki and Imai (2003, their Fig.1) used laboratory experiments to independently developed a diagram similar to the one constructed by Jones and Renaut (1995). Instead of a "disequilibrium factor", they proposed that crystal growth was controlled by a "driving force" that was determined by factors such as supersaturation and supercooling. Their figure shows dendrites developing with a high driving force when diffusion was the dominant process. Irrespective of the nuances involved, both schemes attribute dendrite development to rapid growth under high saturation levels.

The underlying control on precipitation in the Yunnan springs must allow precipitation of the different polymorphs of $CaCO_3$ as well as the growth of the unusual crystal forms, including dendrites. Although this can be attributed to "disequilibrium factor" of Jones and Renaut (1995) or the "driving force" of Oaki and Imai (2003), it seems probable that more than one parameter drives the process, especially given that microbes are present in all of these systems. It is difficult, however, to argue that parameters such as T, Mg content, or the Mg:Ca ratio of the parent water are responsible because the factors that control precipitation must allow variability in mineralogy and crystallography from the sub-millimeter scale to meter scale. In most of the hot springs in the Rehai geothermal area, CO_2 derived from the mantle commonly forms >90% of the gases associated with the hot springs (Liao et al., 1991; Shangguan et al., 2000; Du et al., 2005; Ren et al., 2005; Shangguan et al., 2005). In some springs the CO_2 is known to vary with time (Du et al., 2005) due to (1) hydrothermal explosions (Shangguan et al., 2005), (2)

earthquake activity (Ren et al., 2005), and/or (3) irregular temporal variations in contribution of CO_2 from the atmosphere, crust, and mantle (Du et al., 2005). As spring waters with high CO_2 content flow from their vents there is the potential for rapid degassing that may lead to disequilibrium conditions (e.g., Rodríguez-Berriguete et al., 2012) and the precipitation of aragonite or calcite irrespective of T, Mg content or any other factor. The notion that CO_2 degassing may be the ultimate control on the precipitation of calcite or aragonite may also explain the mineralogical and crystallographic variations that are evident at all temporal and spatial scales.

8. Conclusions

Precipitates in and around active hot spring vent pools in Yunnan Province, including those at Shiqiang, are characterized by mineralogical and crystallographic complexity. Typically, deposits like those at Shiqiang, are formed of (1) calcite and lesser amounts of aragonite that are intercalated with each other at all scales, (2) calcite dendrites of variable size and shape that grew from a solid substrate, (3) spar calcite crystals that grew from a solid substrate, (4) unattached dodecahedral and rhombohedral crystals, commonly with incomplete growth of their faces and edges, that grew in microbial mats, (5) arrays of hexagonal aragonite crystals with a pointed or flat terminus, and crystal twinning, (6) late-phase precipitates that commonly grew over and masked the earlier formed precipitates, and (7) biofilms and their formative microbes that are locally preserved by silicification. Collectively, these features seem to be the hallmark of precipitates that form in the hot springs in Yunnan Province.

The meteoric origin of the modern spring waters from Shiqiang, Eryuan, Gongxiaoshe, Zhuyuan, Jifei, and Rehai, is shown by their δD_{water} and $\delta^{18}O_{water}$ values that plot close to the GMWL and CMWL. The $\delta^{13}C_{travertine}$ values, indicative of thermogene springs as defined by

Pentecost and Viles (1994) and Pentecost (2005), suggests that the spring waters were heated at depth where they derived their CO_2 from the mantle and/or decarbonation with bedrock before mixing with cold groundwater (soil CO_2), to varying degrees, as they ascended to the surface. Precipitation in and around the spring vent pools was probably triggered by rapid CO_2 degassing that produced high levels of supersaturation with respect to $CaCO_3$. Critically, the distribution of the calcite and aragonite does not appear to be linked to water T, Mg content, or Mg/Ca ratio as has commonly been suggested. Instead, the calcite and aragonite precipitation, which was not in isotopic equilibrium with the spring water, was probably controlled, at all scales, by the saturation levels that were controlled by the rate of CO_2 degassing. Although microbial mats probably play influenced precipitation, they were only rarely preserved by local silicification.

Acknowledgments

Samples used in this study were collected with the permission of the owners of the Shiqiang site. Financial support for this research came from the Natural Sciences and Engineering Research Council of Canada (grant No. ZA635 to Jones), the National Natural Science Foundation of China (grants 41172309 and 41272370 to Peng) and the Frontier Project of the Chinese Academy of Sciences (SIDSSE1301 to Peng). We are indebted to George Braybrook who took the SEM images used in this paper, Dr. T. Chacko for discussions regarding the interpretation of the isotope data, Simone Booker who performed some of the isotope analyses, and Diane Caird who undertook the XRD analyses. We are also greatly indebted to Drs. A. Kano, S. Kele, and J. Knight, and provide critical reviews of an earlier version of this paper.

FIGURE CAPTIONS

Fig. 1. Location of study area. (A) Map of China showing location of Tengchong, which is the nearest city to Shiqiang. (B) Location of Shiqiang relative to other springs at Tengchong, Ruidianxiang, Eryuan, and Jifei.

Fig. 2. Views of active springs at Shiqiang. (A) General view to north showing location of springs S1 and S2. (B) Spring S2, surrounded by white tiled ledge and a concrete wall. (C) Edge of S2 pool showing submerged precipitates around wall. (D) General view of vent pool at S1. (E) View of margin around vent pool at S1 showing ledges and green microbial mats. (F) Ledge around vent pool of S1 showing precipitates on ledge that is above water level.

Fig. 3. Thin section photomicrographs of precipitates from spring S1. All plane polarized light. Blue = porosity. A = aragonite, C = calcite. (A) General view showing contrast between the laminated calcite/aragonite, dendrite-A, dendrite-B, and spar calcite zones. Spring pool water on left side. White letters D, E, and H indicate positions of panels D, E, and H, respectively. (B) Laminated zone with bulbous projection. From area just below that shown in panel A. (C) Contrast between the laminated, dendrite-A, and dendrite-B zones. From area just below these zones shown in panel A. White 4C indicates position of Fig. 4C. (D, E) Dendrite B zone showing contrast in morphology of cone-dendrites with cones in panel E having a larger diameter than those in panel D (see panel A for positions). Note growth lines (arrows) defined by thin, dark coloured layers of aragonite. White letter F (panel E) indicates position of panel F. (F) Enlarged view of cone dendrite showing component calcite crystals and branching morphology. (G) Enlarged view of laminated zone showing layers of small calcite crystals. (H) Upper part of laminated zone (see panel A) with laminated, bulbous projection.

Fig. 4. Thin section photomicrographs of precipitates from springs S1 (A-C) and S2 (D-H). All with plane polarized light except for panel B that is with crossed polarized light. Blue = porosity. A = aragonite, C = calcite. (A, B) Spar calcite zone (see Fig. 3A) showing calcite crystals and growth surfaces defined by Fe staining. Note irregular shapes of crystals as evident in crossed polarized light in panel B. (C) Lower part of Dendrite-B zone formed of merged cone-dendrite (compare with Fig. 3D, E). (D) Laminated zone formed of alternating aragonite and calcite laminae. (E-G) Series of images showing same laminations traced laterally over a distance of ~ 4 mm with G being the closest to the spring pool. Note change from aragonite dominated (E) to mixed aragonite-calcite (F) to dominantly calcite (G) over this short distance. (H) Enlarged view from laminated zone showing alternating calcite and aragonite crystals in same micro-laminae.

Fig. 5. SEM photomicrograph of sample from S2 showing thinly laminated aragonite and calcite (right side), coated by largely structureless spar calcite (left), which developed on the pool side of the sample.

Fig. 6. SEM photomicrographs of calcite crystals that form one of the distinct white layers in the precipitates around S1. (A) General view of bundles of calcite crystals with branches growing from basal area. The branches in some bundles are more widely splayed than in others. Note constrictions in crystals that are probably indicative of growth surfaces (black arrows). (B) Enlarged view from left center of panel A showing crystal bundle with widely splayed branches. White letters E and G indicate positions of panels E and G, respectively. (C) Oblique view of sample from top showing base of crystal bundle (top left corner) with branches splayed outwards towards top (right middle). Note circular arrangement of crystals at top of the bundle (right side of image). (D) Top of crystal bundle showing

circular arrangement of crystals. White letter H indicates position of panel H. (E-G) Various views of sides of branches showing stacked, obliquely oriented calcite rhombs. (H) Enlarged view of top of crystal bundle showing small arrays of aragonite (A) crystals between the calcite (C) crystals.

Fig. 7. View of surface of hand specimen of red calcite that forms the outer coating of precipitates around the vent pool. Note numerous circular tubes, of variable diameter, that cut through the precipitates.

Fig. 8. SEM photomicrographs of aragonite from S1 and S2. A = aragonite; C = calcite. (A) General view of substrate showing bundles of radiating aragonite crystals interspersed with euhedral calcite crystals. (B) Bundles of radiating aragonite crystals surrounding a calcite crystal. (C) Sides of hexagonal aragonite crystals showing longitudinal zig-zag suture lines. (D) Group of radiating aragonite crystals showing hexagonal cross-sectional shapes. (E) Aragonite crystals in wheat-sheaf arrangement. (F) Aragonite with large flat bladed section with group of radiating crystals at one end. (G) Bundle of radiating aragonite crystals encased by euhedral calcite crystal. (H) Enlarged view from panel G showing calcite around the aragonite crystals. (I) Enlarged view of aragonite crystals from lower right corner of bundle shown in panel H. (J) Vertical section through bundle of aragonite crystals that was encased by calcite. (K) Enlarged view from panel J showing junction between the calcite and the aragonite.

Fig. 9. SEM photomicrographs of calcite crystals from S2. A = aragonite; C = calcite. (A) General view showing well developed laminae grading from aragonite (upper right) to calcite (middle and lower left). White letters B, C, and D indicate positions of panels B, C, and D). (B) Laminae formed almost entirely of aragonite. (C) Laminae equivalent to those

shown in panel B, but formed of aragonite and small calcite crystals. (D) Laminae equivalent to those shown in panels B and C, but formed largely of calcite (C) crystals with thin laminae formed of aragonite. White letter E indicates position of panel E. (E) Radiating columnar calcite crystals cut by thin laminae of aragonite crystals. (F) Lower part of sample (just below bottom of area shown in panel A) formed almost entirely of radiating calcite crystals. Only minor amounts of aragonite are found in this area. White letter G indicates position of panel G. (G) Enlarged view of calcite crystals that are formed of stacked, inclined rhombs. White letter H indicates position of panel H. (H) Enlarged view of calcite crystals.

Fig. 10. SEM photomicrographs of calcite overgrowths on calcite bundles. (A) Surface of calcite crystals covered with numerous small calcite crystals. (B) Enlarged view of calcite overgrowth crystals with each crystal being formed of numerous nanocrystals. White letter C indicates position of panel C. (C) Mesocrystal formed of numerous nanocrystals. (D) Surface of parent calcite crystal covered by numerous overgrowth crystals. White letter E indicates position of panel E. (E) Enlarged view of overgrowth crystals. White letters F and G indicate positions of panels F and G, respectively. (F, G) Enlarged views of overgrowth mesocrytals. (H, I) Surface of calcite crystal almost totally covered by overgrowth calcite mesocrystal crystals.

Fig. 11. SEM photomicrographs of unattached euhedral calcite crystals from S1 (A-D, F-I) and S2 (E). A = aragonite, C = calcite. (A–C) Dodecahedron calcite crystals exhibiting various stages of development. (D) Rhombic calcite crystal with smooth, well-developed crystal faces. (E) Cluster of euhedral rhombic calcite crystals, partly enmeshed in microbial filaments. (F) Rhombic calcite crystal associated with minor amounts of aragonite crystals.

915 (G-I) Examples of unattached calcite crystals enmeshed in biofilms. Note diatom (D)
916 embedded in biofilm shown in panel G.

917 **Fig. 12.** SEM photomicrographs of Si-Fe precipitates associated with microbes and biofilms.
918 Images from S1 (A-G, J–L) and S2 (H, I). EDX analysis shows that all of the microspheres
919 are formed of Si with minor amounts of Fe. (A) General view of clusters of radiating
920 aragonite crystals overlain by silicified filamentous microbes. White letter B indicates
921 position of panel B. (B) Silicified filamentous microbes resting on top of aragonite crystals.
922 (C) Filamentous microbes coated with Si-Fe microspheres. Note open lumen in filament on
923 right side of image. (D) Hollow filamentous microbe with wall formed of Si and Fe. (E)
924 Cluster of radiating aragonite crystals covered with microspheres. White letters F and G
925 indicate positions of panels F and G, respectively. (F) String of microspheres lying on top
926 of aragonite crystals. (G) Microspheres of various sizes resting on top of aragonite crystals.
927 Note spheres with central hole or slot (lower left corner). (H) Cluster of radiating aragonite
928 crystals covered with thin biofilm. (I) Enlarged view of central part of panel H showing
929 thin biofilm with numerous embedded microspheres. (J, K) Microspheres associated with
930 biofilms. (L) Mineralized filamentous microbes (Si and Fe) overlying cluster of calcite (C)
931 and aragonite (A) crystals.

932 **Fig. 13.** Microbial mat and associated organisms from S1 (K, L) and S2 (A-J). Numerous EDX
933 analyses showed that the microspheres are formed of Si with minor amounts of Fe. (A)
934 Surface microbial mat with microbes embedded in biofilm. (B) Enlarged view of microbes
935 in biofilm. Note microspheres on biofilm surface. (C, D) Cross-sections through biofilm.
936 Note microspheres embedded in biofilm shown in panel D. (E) Enlarged view of cross-
937 section through biofilm showing embedded microspheres. (F) Cross-section through

938 biofilm with dense array of microspheres. (G) Microspheres on surface of biofilm between
939 embedded microbes. White letter H indicates position of panel H. (H) Small diameter
940 silicified filamentous microbe on surface of biofilm partly submerged by microspheres. (I,
941 J) Enlarged views of filamentous microbes coated with microspheres. (K) Example of
942 intact Euglyphida associated with biofilm. (L) Example of intact diatom frustule associated
943 with biofilm.

944 **Fig. 14.** Bivariant graph showing relationship between $\delta^{18}O_{VSMOW}$ and δD_{VSMOW} for the spring
945 waters from Shiqiang, Eryuan, Gongxiaoshe, Zhuyuan, and Jifei relative to the Global
946 Meteoric Water Line (GMWL) and the Chinese Meteoric Water Line (CMWL). GMWL
947 as defined by (Craig, 1961), CMWL as defined by Zheng et al. (2009).

948 **Fig. 15.** Comparison of measured and calculated temperatures for spring waters at Shiqiang (S1
949 and S2), Gongxiaoshe, Zhuyuan, Jifei, and Eryuan. Calculated temperatures, assuming
950 samples formed of calcite, derived using equations developed by Anderson and Arthur
951 (1983), Hays and Grossman (1991), Kim and O'Neil (1997), and O'Neil et al. (1969).
952 Calculated temperatures from Chacko and Deines (2008) show ranges derived by
953 considering samples formed of 100% aragonite and 100% calcite.

954 **Fig. 16.** $\delta^{18}O_{VPDB}$ versus % calcite (as determined from XRD analyses) for spring deposits from
955 Shiqiang (S1 and S2), Jifei, Eryuan, Shuzhisti, Zhuyuan, and Gongxiaoshe. For some
956 springs only point is apparent because all of the samples have relatively consistent
957 $\delta^{18}O_{VPDB}$ and % calcite values. Note lack of correlation between $\delta^{18}O_{VPDB}$ and % calcite.

958 **Fig. 17.** (A) $\delta^{18}O_{VSMOW}$ values for waters collected from springs at Shiqiang (S1 and S2),
959 Eryuan, Jifei, Zhuyuan, Gongxiaoshe, and Shuzhishi. Given that Shuzhishi is no longer an
960 active spring, the value is given as a range (blue line) based on nearby active springs. The

value for the Chemurkeu springs in Kenya (from Renaut and Jones, 1997) are given for comparative purposes. There is no vertical scale for this diagram – spring values are positioned so that they are opposite their $\delta^{18}O_{VSMOW}$ vs $\delta^{13}C_{VPDB}$ values of each spring to allow easier comparisons between the water and precipitate values. (B) Bivariant graph showing comparisons between the $\delta^{18}O_{VSMOW}$ and $\delta^{13}C_{VPDB}$ values for the calcite/aragonite precipitates from the different Yunnan hot springs. The dashed line is derived for the Yunnan spring precipitates. The $\delta^{18}O_{VSMOW}$ and $\delta^{13}C_{VPDB}$ values of the calcite and aragonite precipitates associated with the Chemurkeu springs in Kenya (from Renaut and Jones, 1997) are shown for comparative purposes.

Fig. 18. Comparison of $\delta^{18}O_{VSMOW}$ and $\delta^{13}C_{VPDB}$ values from Chinese spring deposits (this paper) and Kenyan springs (from Renaut and Jones, 1997, their Fig. 8) with those from various Hungarian springs as shown by Kele et al. (2008, their Fig. 13). Ranges for thermogene and meteogene springs based on $\delta^{13}C_{VPDB}$ values, as defined by Pentecost (2005).

REFERENCES

Anderson, T.F., Arthur, M.A., 1983. Stable isotopes of oxygen and carbon and their application to sedimentologic and palaeoenvironmental problems. In: Arthur, M.A., Anderson, T.F., Kaplan, I.R., Veizer, J., Land, L.S. (Eds.), Stable Isotopes in Sedimentary Geology. Society of Economic Paleontologists and Mineralogists, Tulsa, Oklahoma, pp. 1.1-1.151.

Beck, W.C., Grossman, E.L., Morse, J.W., 2005. Experimental studies of oxygen isotope fractionation in the carbonic acid system at 15°, 25°, and 40°C. Geochimica et Cosmochimica Acta 69, 3493-3503.

Bottinga, Y., 1968. Calculations of fractionation factors for carbon and oxygen isotopic exchange in the system calcite-carbon dioxide-water. Journal of Physical Chemistry 72, 800-808.

Brinkley, K.L., Wilkinson, B.H., Owen, R.M., 1980. Vadose beachrock cementation along a southeastern Michigan marl lake. Journal of Sedimentary Petrology 50, 953-962.

Buckley, H.E., 1951. Crystal Growth. John Wiley and Sons Inc., London, 359 pp.

Chacko, T., Cole, D.R., Horita, J., 2001. Equilibrium oxygen, hydrogen and carbon isotope fractionation factors applicable to geological systems. In: Valley, J.W., Cole, D.R. (Eds.), Reviews in Mineralogy and Geochemistry, pp. 1-81.

Chacko, T., Deines, P., 2008. Theoretical calculation of oxygen isotope fractionation factors in carbonate systems. Geochimica et Cosmochimica Acta 72, 3642-3660.

Chacko, T., Mayeda, T.K., Clayton, R.N., Goldsmith, J.R., 1991. Oxygen and carbon isotope fractionations between CO_2 and calcite. Geochimica et Cosmochimica Acta 55, 2867-2882.

Chafetz, H.S., Wilkinson, B.H., Love, K.M., 1985. Morphology and composition of non-marine carbonate cements in near-surface settings. In: Schneidermann, N., Harris, P.M. (Eds.),

Carbonate Cements. Society of Economic Paleontologists and Mineralogists, Special Publication 36, pp. 337-347.

Cheng, Z., Guo, Z., Zhang, M., Zhang, L., 2014. Carbon dioxide emission from Tengching Cenozoic volcanic field, Yunnan Province, SW China. Acta Petrologica Sinica 30, 3657-3670.

Cölfen, H., Antonietti, M., 2005. Mesocrystals: inorganic superstructures made by highly parallel crystallization and controlled alignment. Angewandte Chemie 44, 5576-5591.

Coplen, T.B., 2007. Calibration of the calcite-water oxygen-isotope geothermometer at Devils Hole, Nevada, a natural laboratiry. Geochimica et Cosmochimica Acta 71, 3948-3957.

Craig, H., 1953. The geochemistry of the stable carbon isotopes. Geochimica et Cosmochimica Acta 3, 53-92.

Craig, H., 1961. Isotopic variations in meteoric waters. Science 133, 1702-1703.

De Choudens-Sánchez, V., González, L.A., 2009. Calcite and aragonite precipitation under controlled instantaneous supersaturation: elucidating the role of $CaCO_3$ saturation state and Mg/Ca ratio on calcium carbonate polymorphism. Journal of Sedimentary Research 79, 363-376.

Du, J., Cheng, W., Zhang, Y., Jie, C., Guan, Z., Liu, W., Bai, L., 2006. Helium and carbon isotopic compositions of thermal springs in the earthquake zone of Sichuan, soouthwestern China. Journal of Asian Earth Sciences 26, 533-539.

Du, J., Liu, C., Fu, B., Ninomia, Y., Zhang, Y., Wang, C., Wang, H., Sun, Z., 2005. Variations of geothermometry and chemical-isotope compositions of hot spring fluids in the Rehai geothermal field, southwestern China. Journal of Volcanology and Geothermal Research 142, 243-261.

Emrich, K., Ehhalt, D.H., Vogel, J.C., 1970. Carbon isotope fractionation during the precipitation of calcium carbonate. Earth and Planetary Science Letters 8, 363-371.

Folk, R.L., 1974. The natural history of crystalline calcium carbonate: Effect of magnesium content and salinity. Journal of Sedimentary Petrology 44, 40-53.

Folk, R.L., 1994. Interaction between bacteria, nannobacteria, and mineral precipitation in hot springs of central Italy. Geographie physique et Quaternaire 48, 233-246.

Fouke, B.W., Farmer, J.D., Des Marais, D.J., Pratt, L., Sturchio, N.C., Burns, P.C., Discipulo, M.K., 2000. Depositional facies and aqueous-solid geochemistry of travertine-depositing hot springs (Angel Terrace, Mammoth Hot Springs, Yellowstone National Park, USA). Journal of Sedimentary Research 70, 565-585.

Given, R.K., Wilkinson, B.H., 1985. Kinetic control of morphology, composition and mineralogy of abiotic sedimentary carbonates. Journal of Sedimentary Petrology 55, 109-119.

Greer, H.F., Zhou, W., Guo, L., 2015. Phase transformation of Mg-calcite to aragonite in active-forming hot spring travertines. Mineralogy and Petrology 109, 453-462.

Guo, L., Riding, R., 1992. Aragonite laminae in hot water travertine crusts, Rapolano Terme, Italy. Sedimentology 39, 1067-1079.

Guo, Q., Wang, Y., 2012. Geochemistry of hot springs in the Tengchong hydrothermal areas, Southwestern China. Journal of Volcanology and Geothermal Research 215-216, 61-73.

Hays, P.D., Grossman, E.L., 1991. Oxygen isotopes in meteroic calcite cements as indicators of continental palaeoclimate. Geology 19, 441-444.

Hill, P.S., Schauble, E.A., Tripati, A.K., 2014. Theoretical constraints on the effects of pH, salinity, and temperature on clumped isotope signatures of dissolved inorganic carbon

species and precipitting carbonate minerals. Geochimica et Cosmochimica Acta 125, 610-652.

Hulston, J.R., McCabe, W.J., 1962. Mass spectrometer measurements in the thermal areas of New Zealand. Geochimica et Cosmochimica Acta 26, 399-410.

Jones, B., 1989. Syntaxial overgrowths on dolomite crystals in the Bluff Formation, Grand Cayman, British West Indies. Journal of Sedimentary Petrology 59, 839-847.

Jones, B., Kahle, C.F., 1986. Dendritic calcite crystals formed by calcification of algal filaments in a vadose environment. Journal of Sedimentary Petrology 56, 217-227.

Jones, B., Peng, X., 2012a. Amorphous calcium carbonate associated with biofilms in hot springs. Sedimentary Geology 269-270, 58-68.

Jones, B., Peng, X., 2012b. Intrinsic versus extrinsic controls on the development of calcite dendrite bushes, Shuzhishi Spring, Rehai geothermal area, Tengchong, Yunnan Province, China. Sedimentary Geology 249-250, 45-62.

Jones, B., Peng, X., 2014a. Hot spring deposits on a cliff face: A case study from Jifei, Yunnan Province, China. Sedimentary Geology 302, 1-28.

Jones, B., Peng, X., 2014b. Signatures of biologically influenced $CaCO_3$ and Mg-Fe silicate precipitation in hot springs: Case study from the Ruidian geothermal area, Western Yunnan Province, China. Sedimentology 61, 56-89.

Jones, B., Renaut, R.W., 1995. Noncrystallographic dendrites from hot-spring deposits at Lake Bogoria, Kenya. Journal of Sedimentary Research A65, 154-169.

Jones, B., Renaut, R.W., 1996. Morphology and growth of aragonite crystals in hot-spring travertines at Lake Bogoria, Kenya Rift Valley. Sedimentology 43, 323-340.

Jones, B., Renaut, R.W., Owen, R.B., Torfason, H., 2005. Growth patterns and implications of complex dendrites in calcite travertines from Lýsuhóll, Snæfellsnes, Iceland. Sedimentology 52, 1277-1301.

Kearey, P., Wei, H., 1993. Geothermal fields of China. Journal of Volcanology and Geothermal Research 56, 415-428.

Kele, S., Breitenbach, S.F.M., Capezzuoli, E., Meckler, A.N., Ziegler, M., Millan, I.M., Kluge, T., Deák, J., Hanselmann, K., John, C.M., Yan, H., Liu, Z., Bernasconi, S.M., 2015. Temperature dependence of oxygen- and clumped isotope fractionation in carbonates: A study of travertines and tufas in the 6–95°C temperature range. Geochimica et Cosmochimica Acta 168, 172-192.

Kele, S., Demény, A., Siklósy, Z., Németh, T., Tóth, M., Kovács, M.B., 2008. Chemical and stable isotope composition of recent hot-water travertines and associated thermal waters, from Egerszalók, Hungary: Depositional facies and non-equilibrium fractionation. Sedimentary Geology 211, 53-72.

Kele, S., Özkul, M., Fórizs, I., Gökgöz, A., Baykara, M.O., Alçiçek, M.C., Németh, T., 2011. Stable isotope geochemical study of Pamukkale travertines: New evidences of low-temperature non-equilibrium calcite-water fractionation. Sedimentary Geology 238, 191-212.

Kim, S.-T., O'Neil, J.R., 1997. Equilibrium and nonequilibrium oxygen isotope effects in synthetic carbonates. Geochimica et Cosmochimica Acta 61, 3461-3475.

Kitano, Y., 1955. Chemical investigations of hot springs in Japan. The conditions under which aragonite and calcite are formed. Nippon Kagaku Zassi 75, 581-584 [in Japanese].

Kitano, Y., 1962a. A study of the polymorphic formation of calcium carbonate in thermal springs with an emphasis of the effect of temperature. Journal of Earth Sciences, Nagoya University 35, 1980-1985.

Kitano, Y., 1962b. The behavior of various inorganic ions in the separation of calcium carbonate from a bicarbonate solution. Bulletin of the Chemical Society of Japan 35, 1973-1980.

Kitano, Y., Park, K., Hood, D.W., 1962. Pure aragonite synthesis. Journal of Geophysical Research 67, 4873-4874.

Li, R., Jones, B., 2014. Calcareous crusts on exposed Pleistocene limestones: A case study from Grand Cayman, British West Indies. Sedimentary Geology 299, 88-105.

Liao, Z., Minzi, S., Guoying, G., 1991. Characteristics of the reservoir of the Rehai geotehrmal field in Tengchong, Yunnan Province, China. Acta Geologica Sinica 4, 307-320.

Liu, Y., Zhou, X., Deng, Z., Fang, B., Tsutomu, Y., Zhao, J.X., Wang, X., 2015. Hydrochemical characteristics and genesis analysis of the Jifei hot spring in Yunnan, southwestern China. Geothermics 53, 38-45.

Magdans, U., Gies, H., 2004. Single crystal structure analysis of sea urchin spine calcites: Systematic investigations of the Ca/Mg distribution as a function of habitat of the sea urchin and sample location in the spine. European Journal of Mineralogy 16, 261-268.

Meigen, W., 1901. Eine einfache Reaktion zue unterscheidung von aragonit und kalkspath. Zentralblatt fuer Mineralogie, Geologie, und Paleontologie 1901, 577-578.

Meldrum, F.C., Cölfen, H., 2008. Controlling mineral morphologies and structures in biological and synthetic systems. Chemical Reviews 108, 4332-4432.

O'Neil, J., Clayton, R., Mayeda, T., 1969. Oxygen isotope fractionation in divalent metal carbonates. Journal of Chemical Physics 51, 5547-5558.

Oaki, Y., Imai, Y., 2003. Experimental demonstration for the morphological evolution of crystals grown in gel media. Crystal Growth and Design 3, 711-716.

Okumura, T., Takashima, C., Kano, A., 2013. Textures and processes of laminated travertines formed by unicelluar cyanobacteria in Myokwn hot spring, southwestern Japan. Island Arc 22, 410-426.

Owen, R.B., Renaut, R.W., Jones, B., 2008. Geothermal diatoms: a comparative study of floras in hot spring systems of Iceland, New Zealand, and Kenya. Hydrobiologia 610, 175-192.

Panichi, C., Tongiorgi, E., 1976. Carbon isotopic composition of CO_2 from springs, fumaroles, mofettes and travertines of central and southern Italy: A preliminary prospection method of geothermal areas, Proceedings 2nd U.N. Synposium on the Development and Use of Geothermal Energy, San Francisco, pp. 815-825.

Parkhurst, D.L., Appelo, C.A.J., 1999. User's guide to PHREEQC (version 2) – a computer program for speciation, reaction-path, 1D-transport, and inverse geochemical calculations United States Geological Survey, Water Resource Investigations Report 99-4259, 1-312.

Peng, X., Jones, B., 2013. Patterns of biomediated $CaCO_3$ crystal bushes in hot spring deposits. Sedimentary Geology 294, 105-117.

Pentecost, A., 2005. Travertine. Springer, Berlin Heidelberg, 445 pp.

Pentecost, A., Jones, B., Renaut, R.W., 2003. What is a hot spring? Canadian Journal of Earth Sciences 40, 1443-1446.

Pentecost, A., Viles, H., 1994. A review and reassessment of travertine classification. Geographie physique et Quaternaire 48, 305-314.

Ren, J., Wang, X., Ouyang, Z., 2005. Mantle-derived CO_2 in hot springs of the Rehai geothermal field, Tengchong, China. Acta Geologica Sinica 79, 426-431.

Renaut, R.W., Jones, B., 1997. Controls on aragonite and calcite precipitation in hot spring travertines at Chemurkeu, Lake Bogoria, Kenya. Canadian Journal of Earth Sciences 34, 801-814.

Renaut, R.W., Jones, B., 2000. Microbial precipitates around continental hot springs and geysers. In: Riding, R.E., Awramik, S.M. (Eds.), Microbial Sediments. Springer-Verlag, Berlin Heidelberg, pp. 187-195.

Renaut, R.W., Jones, B., Tiercelin, J.-J., 1998. Rapid *in situ* silicification of microbes at Loburu hot springs, Lake Bogoria, Kenya Rift Valley. Sedimentology 45, 1083-1103.

Rimondi, V., Costagliola, P., Ruggieri, G., Benvenuti, M., Boschi, C., Brogi, A., Capezzuoli, E., Morelli, M., Gasparon, M., Liotta, D., 2016. Investigating fossil hydrothermal systems by means of fluid inclusions and stable isotopes in banded travertine: An example from Castelnuovo dell'Abate (southern Tuscany, Italy). International Journal of Earth Sciences 105, 659-679.

Rodríguez-Berriguete, A., Alonso-Zarza, A.M., Cabrera, M.C., Rodriguez-Gonzalez, A., 2012. The Azuaje Travertine: An example of aragonite deposition in a recent volcanic setting, N Gran Canaria Island, Spain. Sedimentary Geology 277-278, 61-71.

Romanek, C.S., Grossman, E.L., Morse, J.W., 1992. Carbon isotope fractionatoin in synthetic aragonite and calcite: Effects of temperature and precipitation rate. Geochimica et Cosmochimica Acta 56, 419-430.

Sandberg, P., 1985. Aragonite cements and their occurrence in ancient limestones. In: Schneidermann, N., Harris, P.M. (Eds.), Carbonate Cements. Society of Economic Paleontologists and Mineralogists Special Publication No. 36, pp. 33-57.

Shangguan, Z., Bai, C., Sun, M., 2000. Mantle-derived magmatic gas releasing features at Rehai area, Tengchong County, Yunnan Province, China. Science China (Series D) 43, 132-140.

Shangguan, Z., Zhao, C., Li, H., Gao, Q., Sun, M., 2005. Evolution of hydrothermal explosions at Rehai geothermal field, Tengchong volcanic region, China. Geothermics 34, 58-526.

Shi, Z., Shi, Z., Tin, G., Liang, J., 2014. Travertine deposits, deep thermal metamorphism and tectonic activity in the Longmenshan tectonic region, southwestern China. Tectonophysics 633, 156-163.

Suganuma, I., 1928. On the constitutents and genesis of a few minerals produced from hot springs and their vicinities in Japan. III. Calcium carbonate minerals deposited from effervescent springs. Bulletin of the Chemical Society of Japan 3, 87-89.

Towe, K.M., Cifelli, R., 1967. Wall ultrastructure in the calcareous foraminifera. Journal of Paleontology 41, 742-762.

Waring, G.A., 1965. Thermal springs of the United States and other countries of the world – A summary, United States Geological Survey Professional Paper 492, pp. 383.

Zeebe, R.E., 2007. An explanation of the effect of seawater carbonate concentrates on foraminiferal oxygen isotopes. Geochimica et Cosmochimica Acta 63, 2001-2007.

Zhang, G., Liu, C., Liu, H., Jin, Z., Han, G., Li, L., 2008. Geochemistry of the Rehai and Ruidan geothermal waters, Yunnan Province, China. Geothermics 37, 73-83.

Zheng, S., Hou, F., Ni, B., 1983. Hydrogen and oxygen isotopic studies of meteoric water in China. Chinese Scientific Bulletin 28, 801-806. [in Chinese].

Zhou, X., Fang, B., Zhou, H., Li, J., Wang, Y., 2009. Isotopes of deuterium and oxygen-18 in thermal groundwater in China. Environmental Geology 57, 1807-1814.

Zhou, X., Wang, W., Chen, Z., Yi, L., Liu, L., Xie, C., Cui, Y., Du, J., Cheng, J., Yang, L.K., 2015. Hot spring gas geochemistry in western Sichuan Province, China after the Wenchuan Ms 8.0 earthquake. Terrestrial, Atmospheric and Ocedanic Sciences 26, 361-373.

Zhu, M., Tong, W., 1987. Surface hydrothermal minerals and their distribution in the Tengchong geothermal area, China. Geothermics 16, 181-195.

Figure 1
Click here to download high resolution image

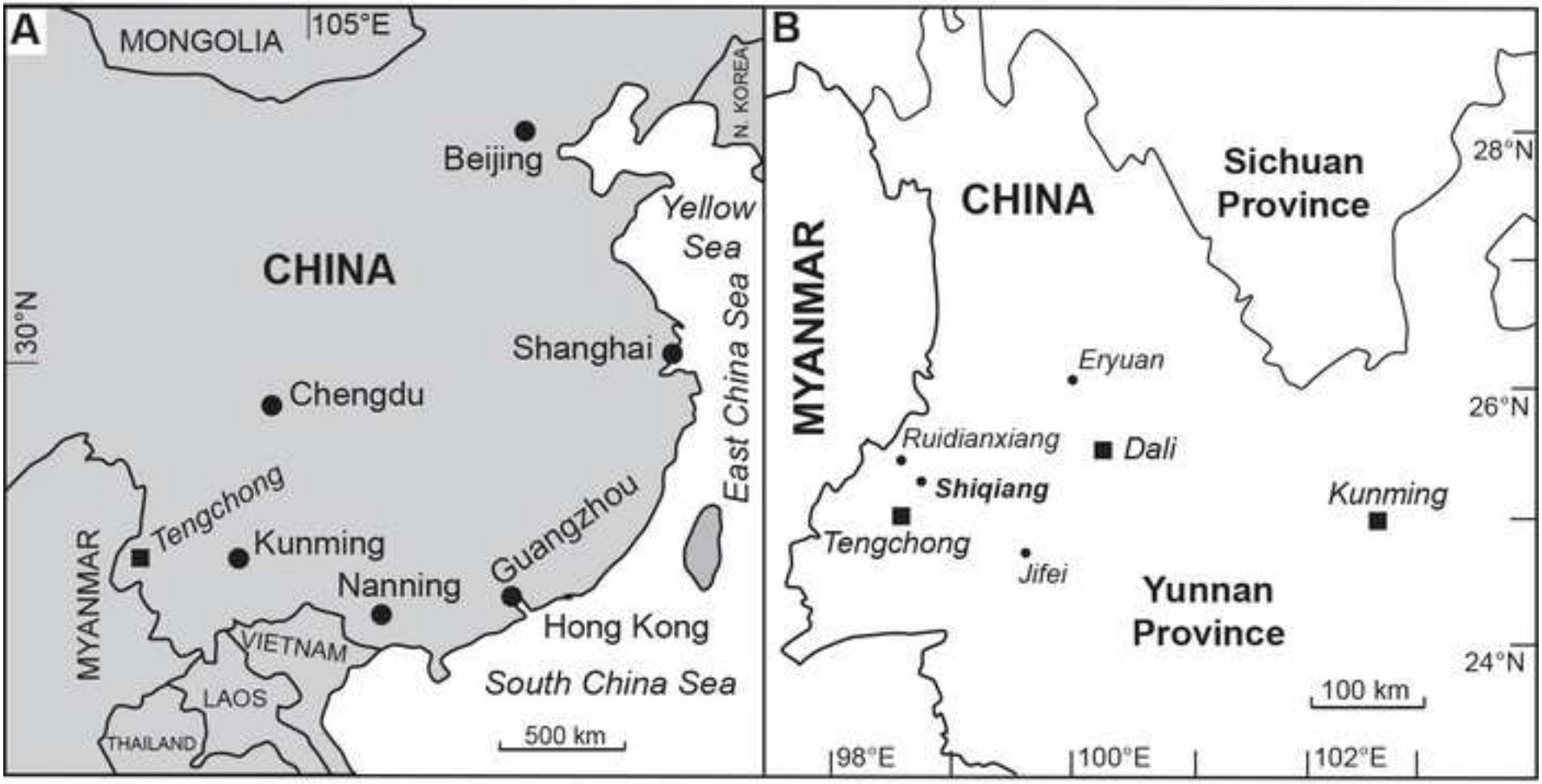

Figure 2
Click here to download high resolution image

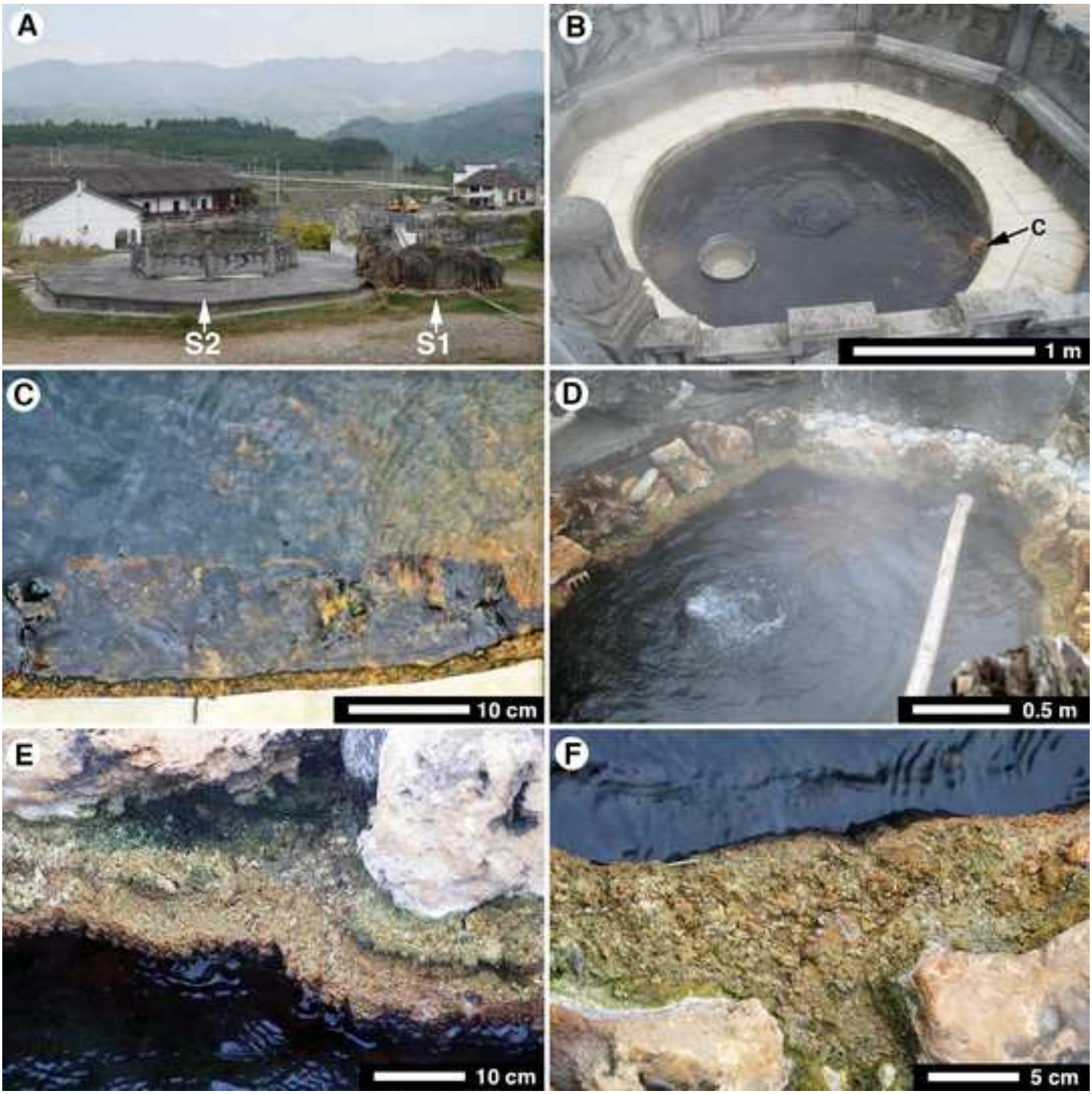

Figure 3
Click here to download high resolution image

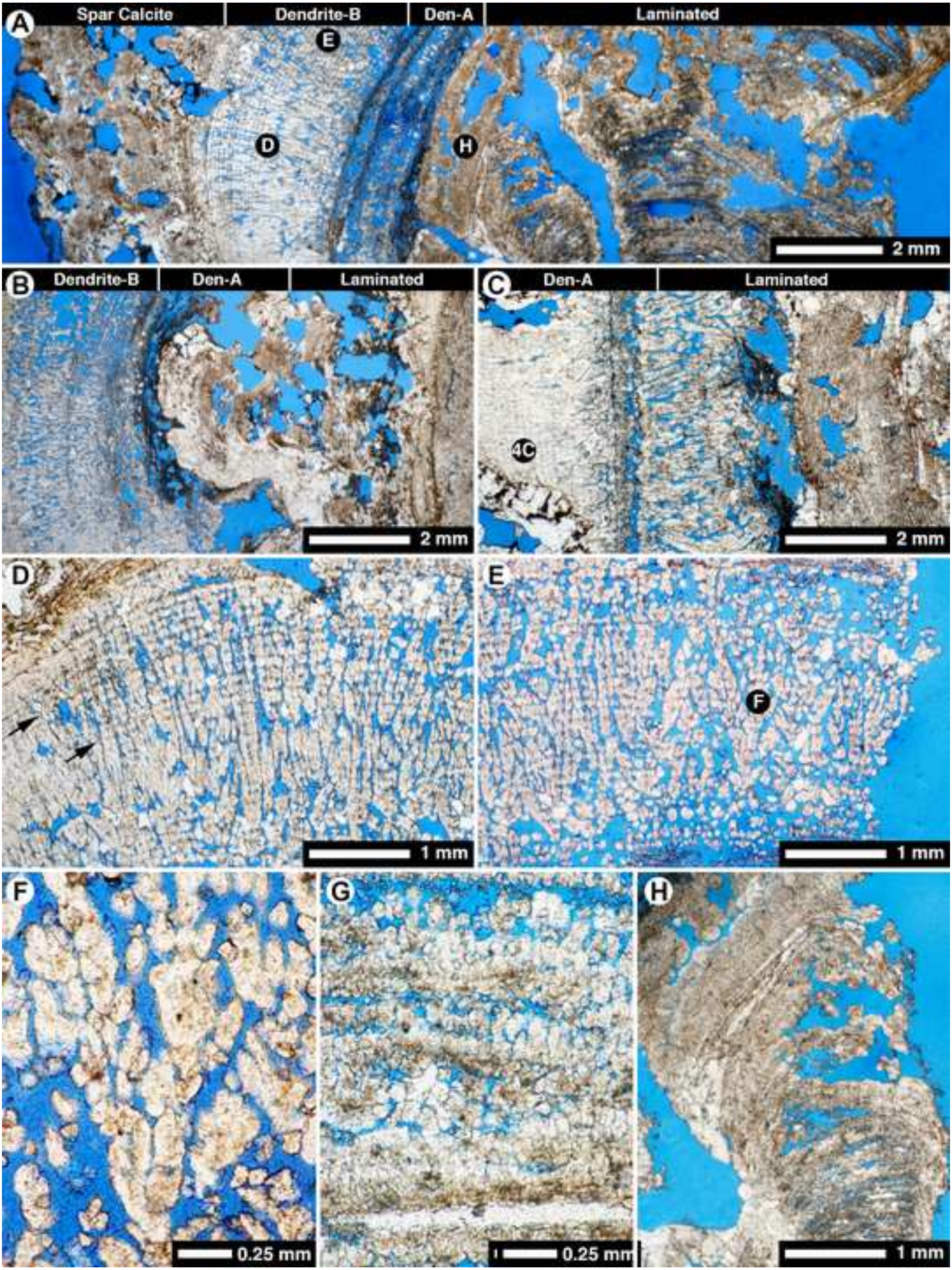

Figure 4
Click here to download high resolution image

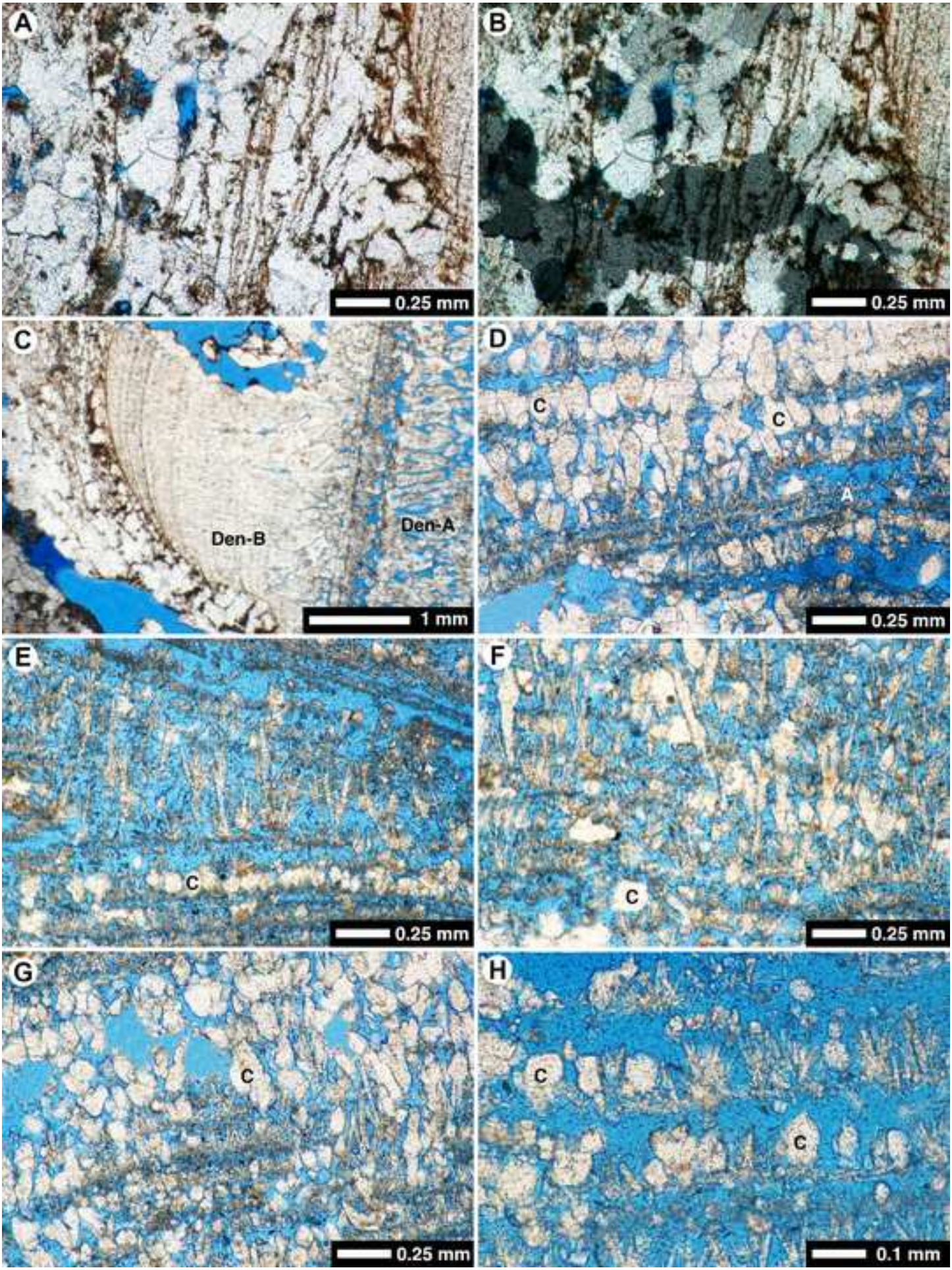

Figure 5
Click here to download high resolution image

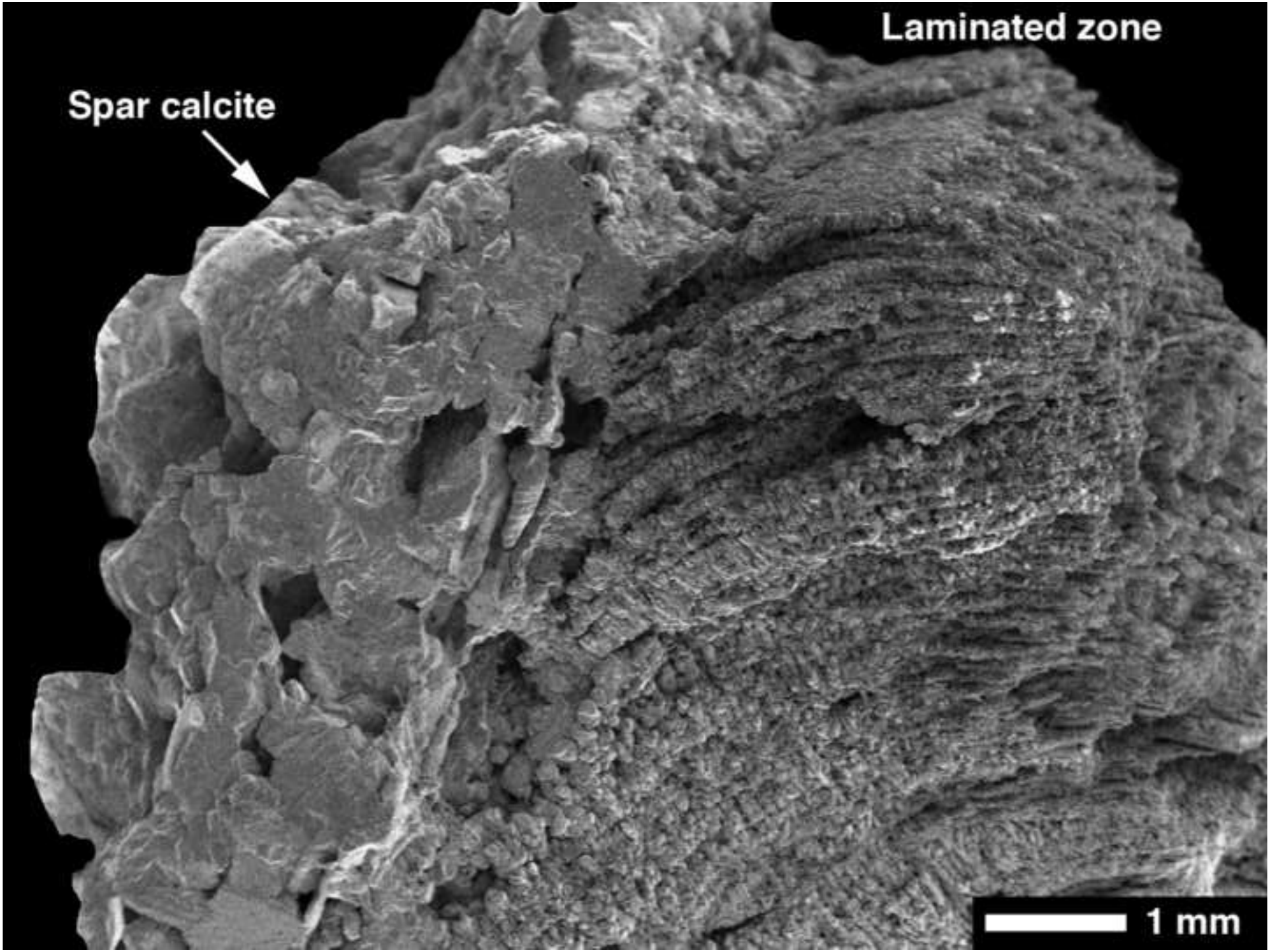

Figure 6
Click here to download high resolution image

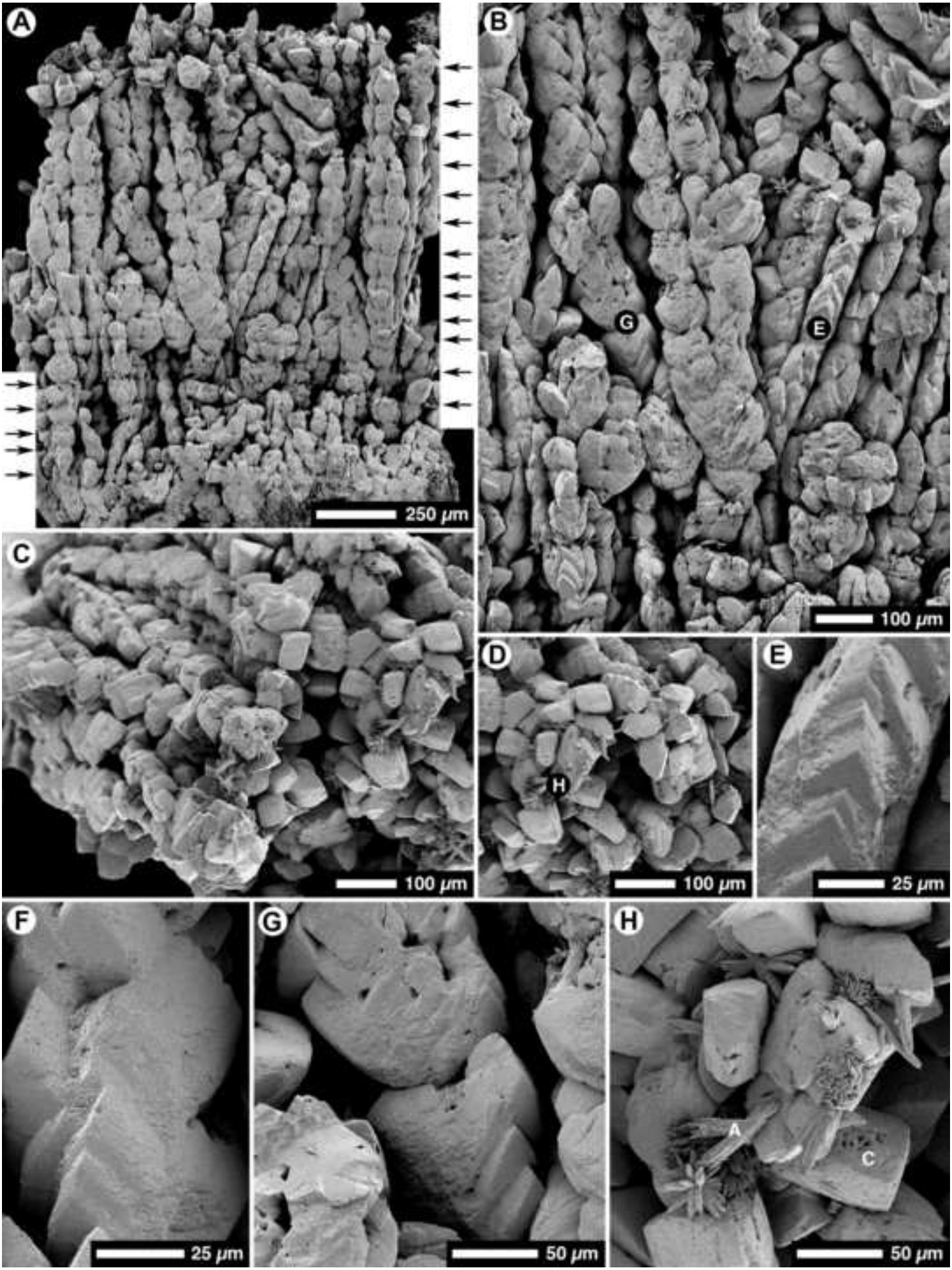

Figure 7
Click here to download high resolution image

Figure 8
Click here to download high resolution image

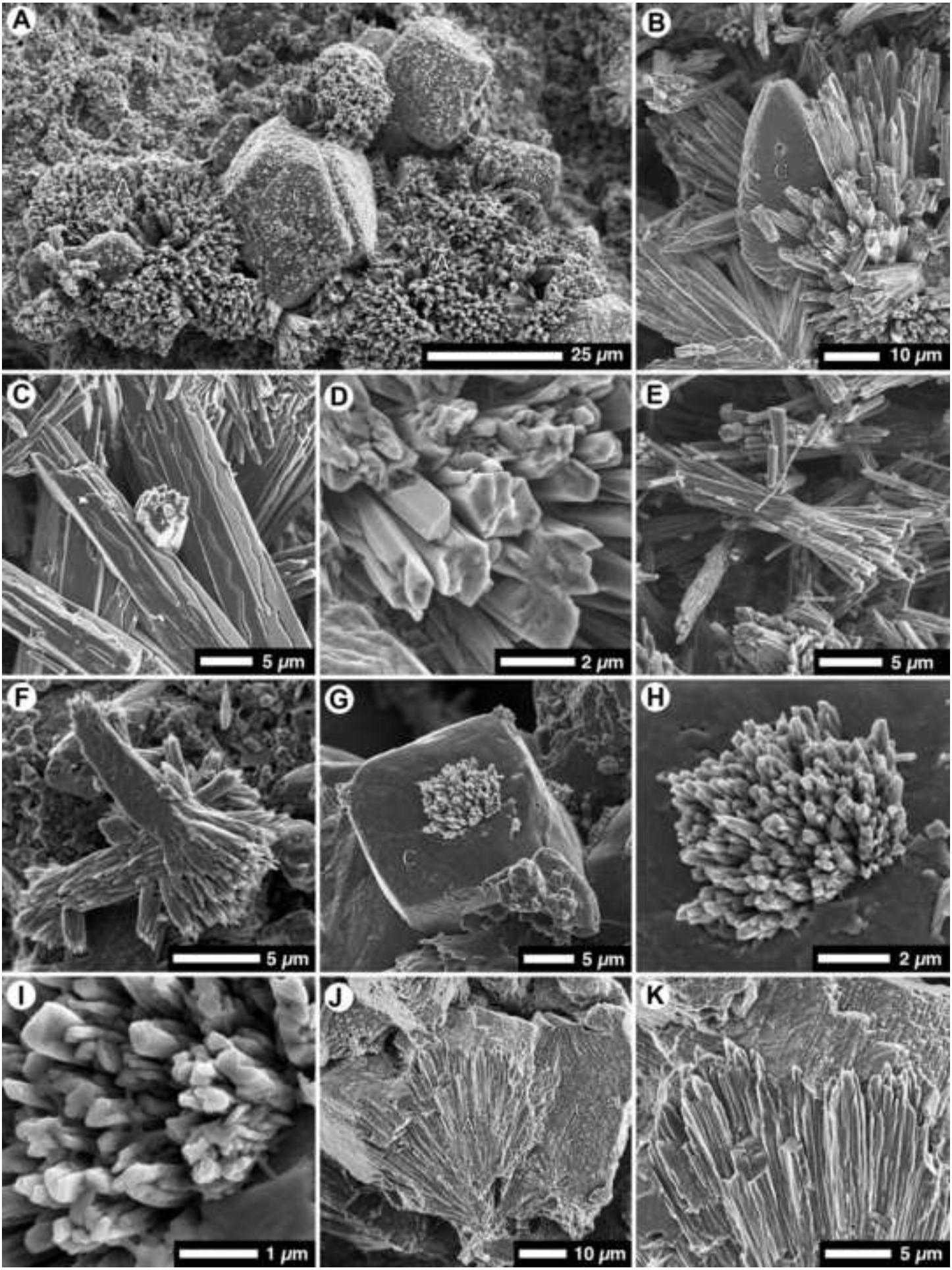

Figure 9
Click here to download high resolution image

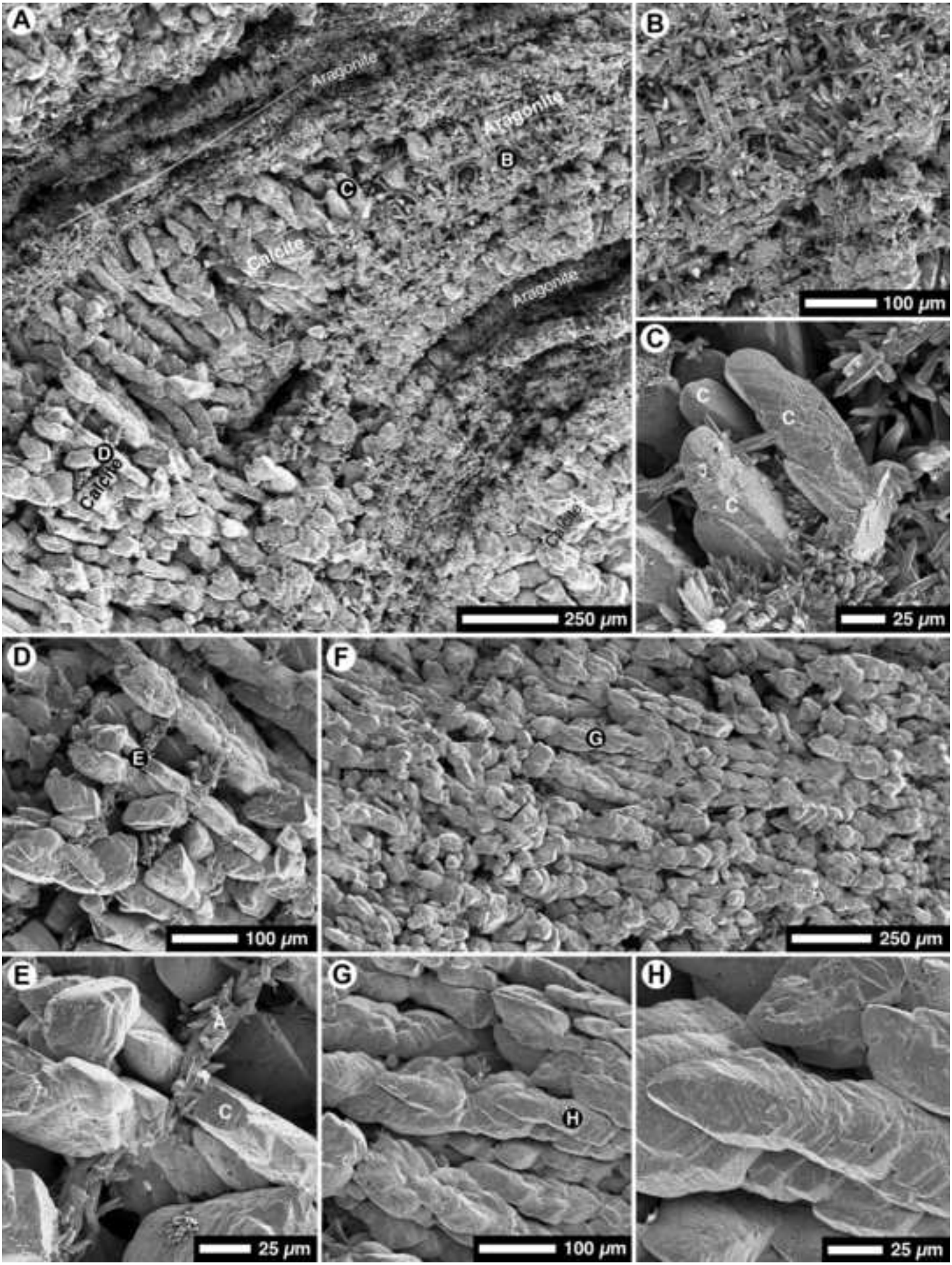

Figure 10
Click here to download high resolution image

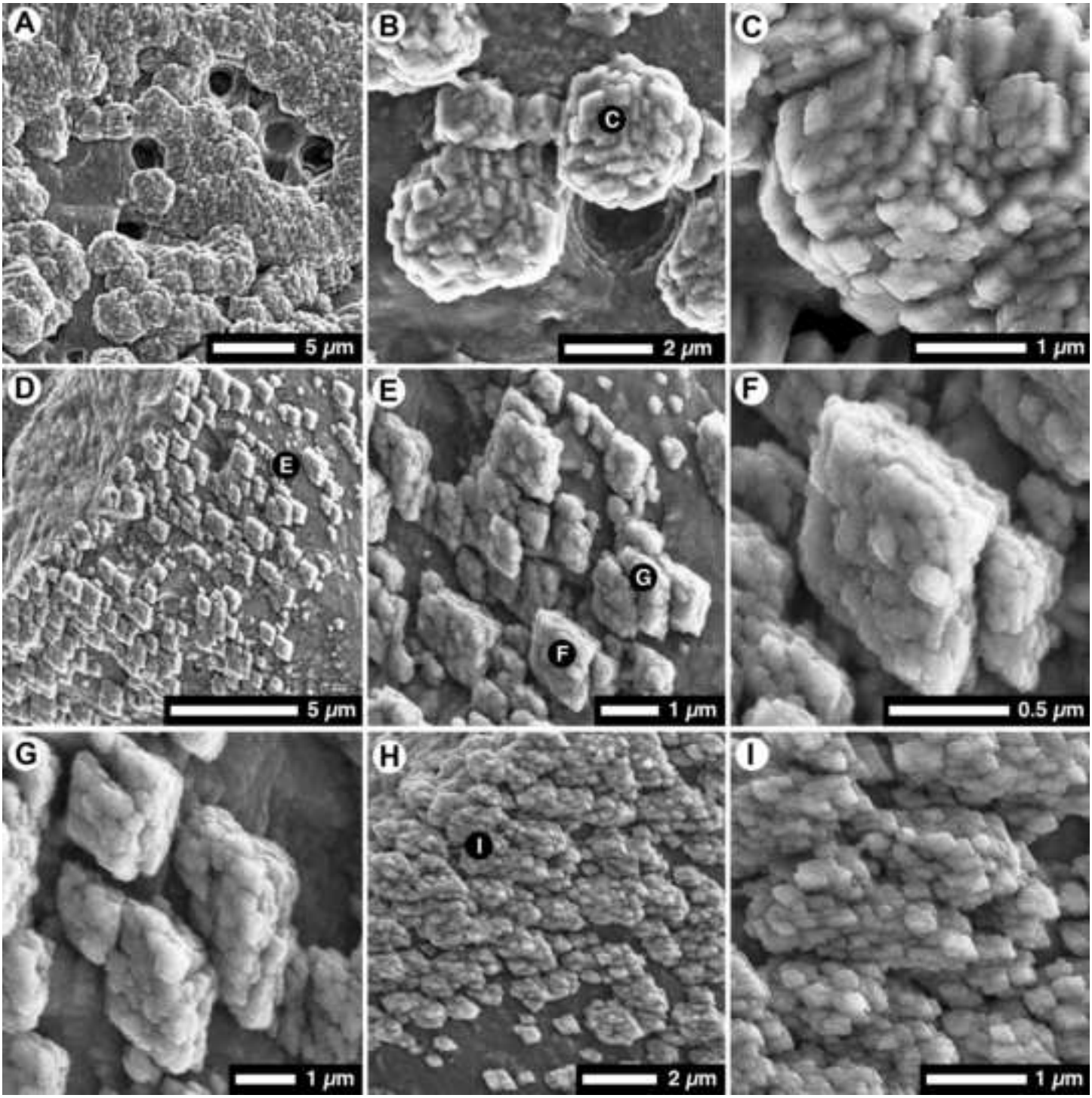

Figure 11
Click here to download high resolution image

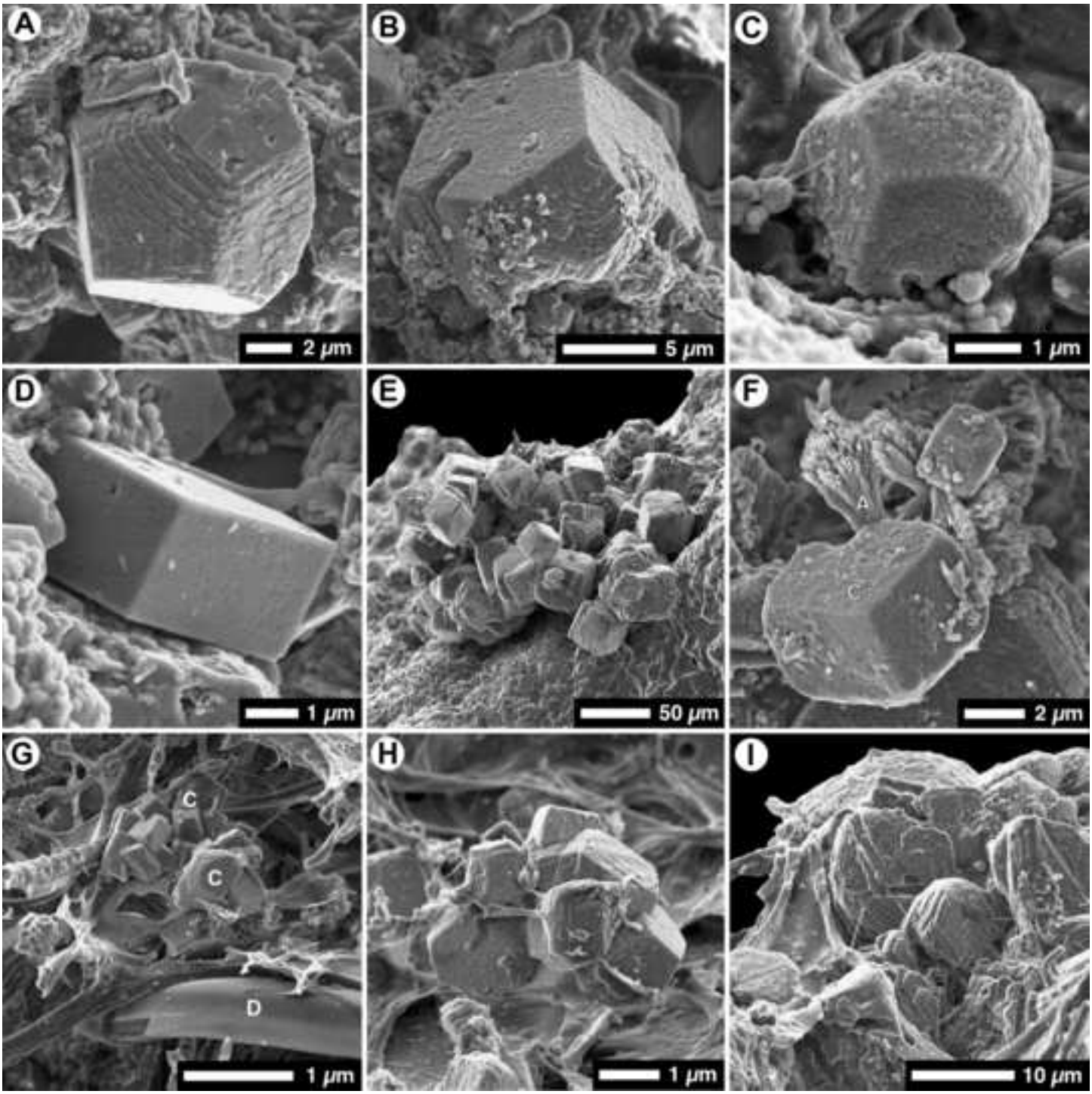

Figure 12
Click here to download high resolution image

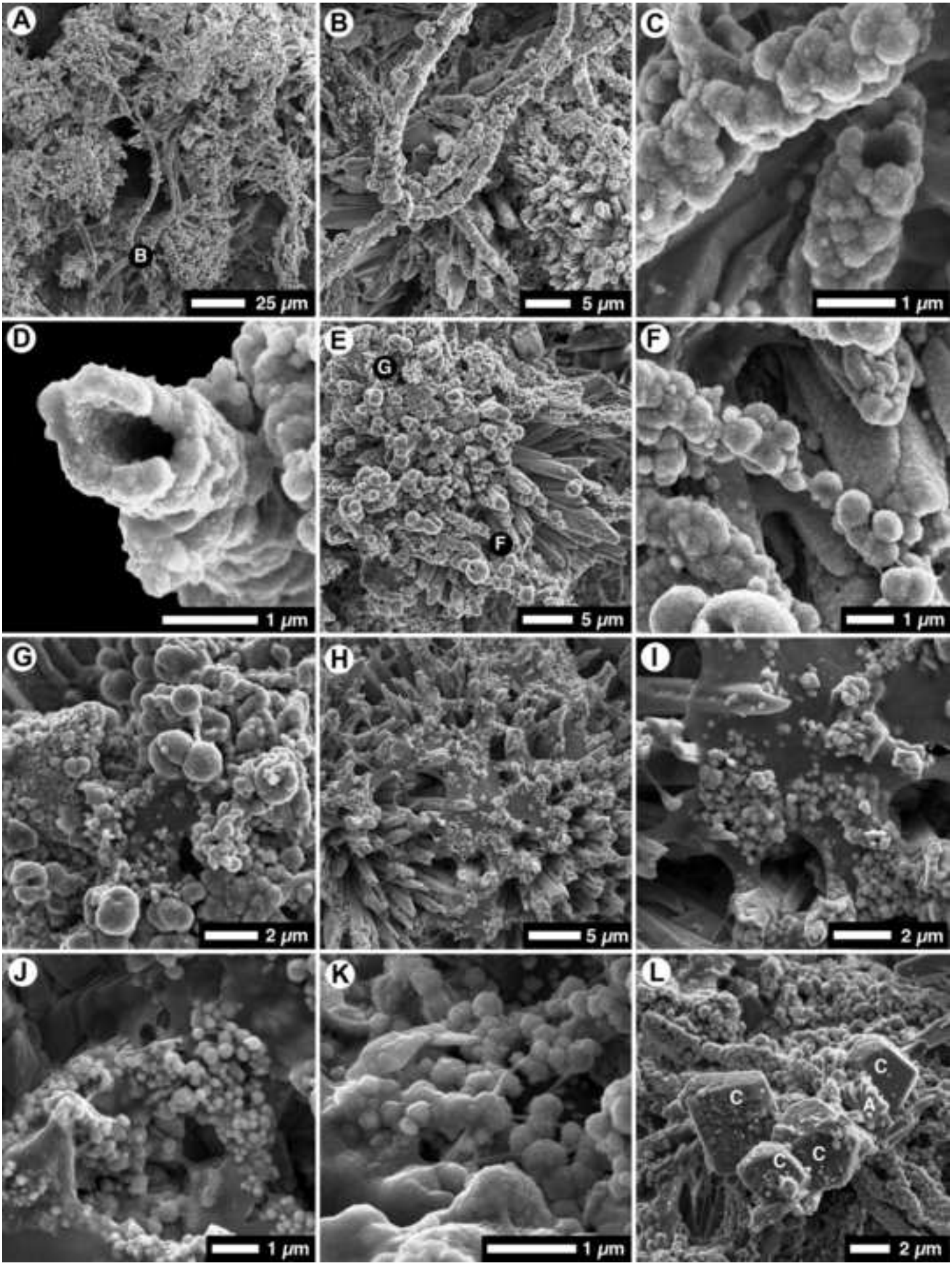

Figure 13
Click here to download high resolution image

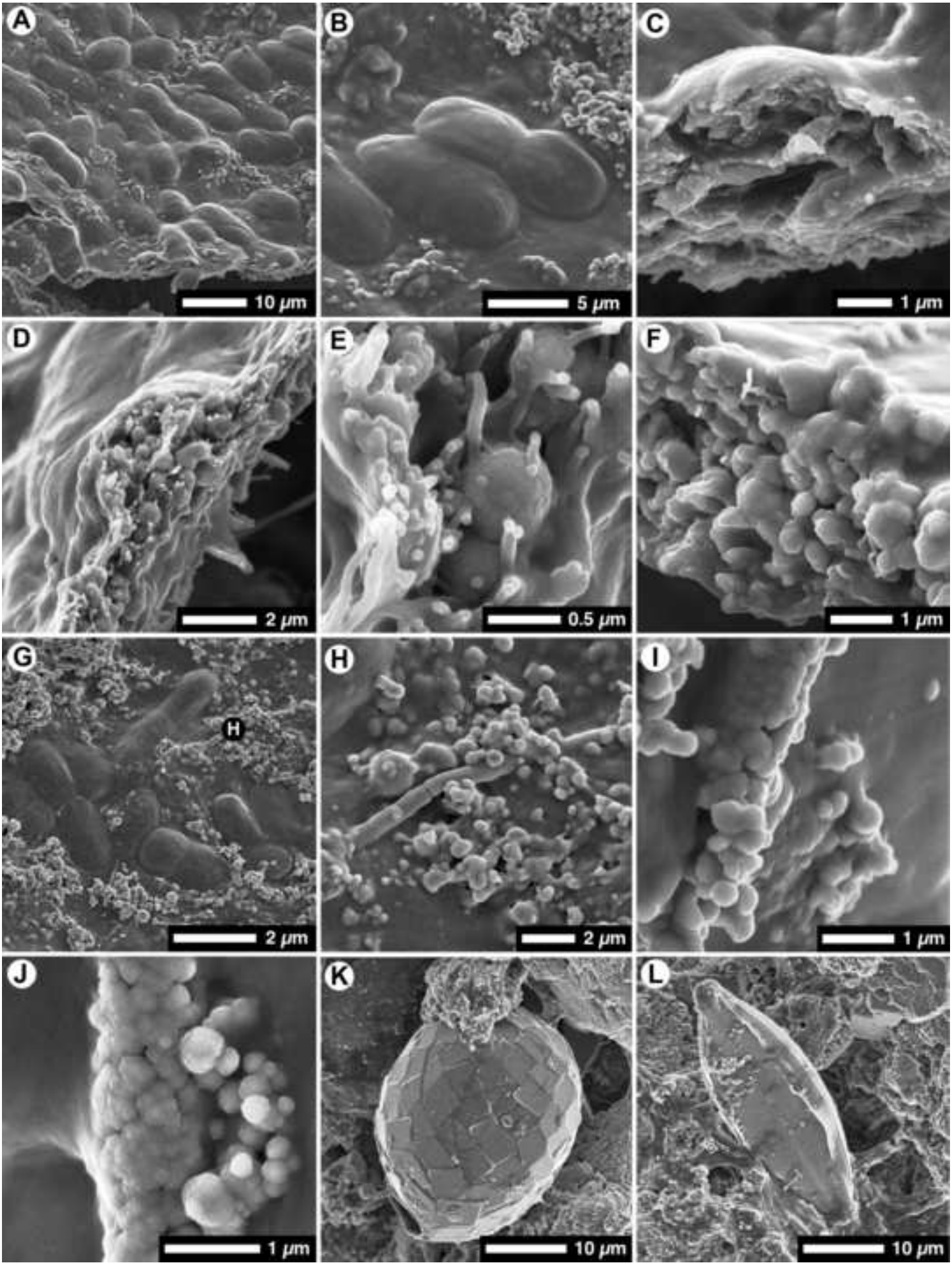

Figure 15

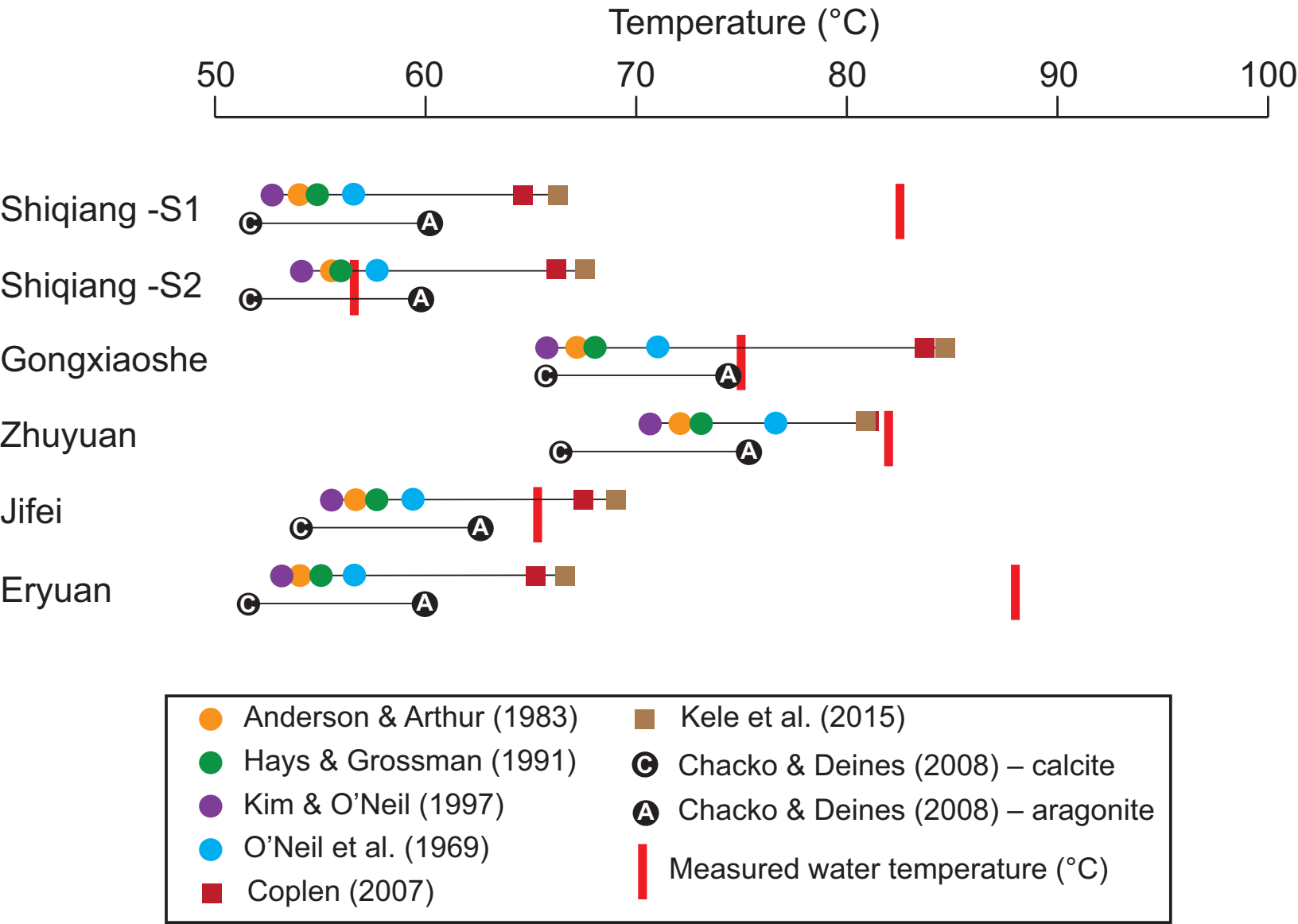
Temperature (°C)
50
60
70
80
90
100
Shiqiang -S1
Shiqiang -S2
Gongxiaoshe
Zhuyuan
Jifei
Eryuan
Anderson & Arthur (1983)
Hays & Grossman (1991)
Kim & O'Neil (1997)
O'Neil et al. (1969)
Coplen (2007)
Kele et al. (2015)
Chacko & Deines (2008) – calcite
Chacko & Deines (2008) – aragonite
Measured water temperature (°C)

Figure 16

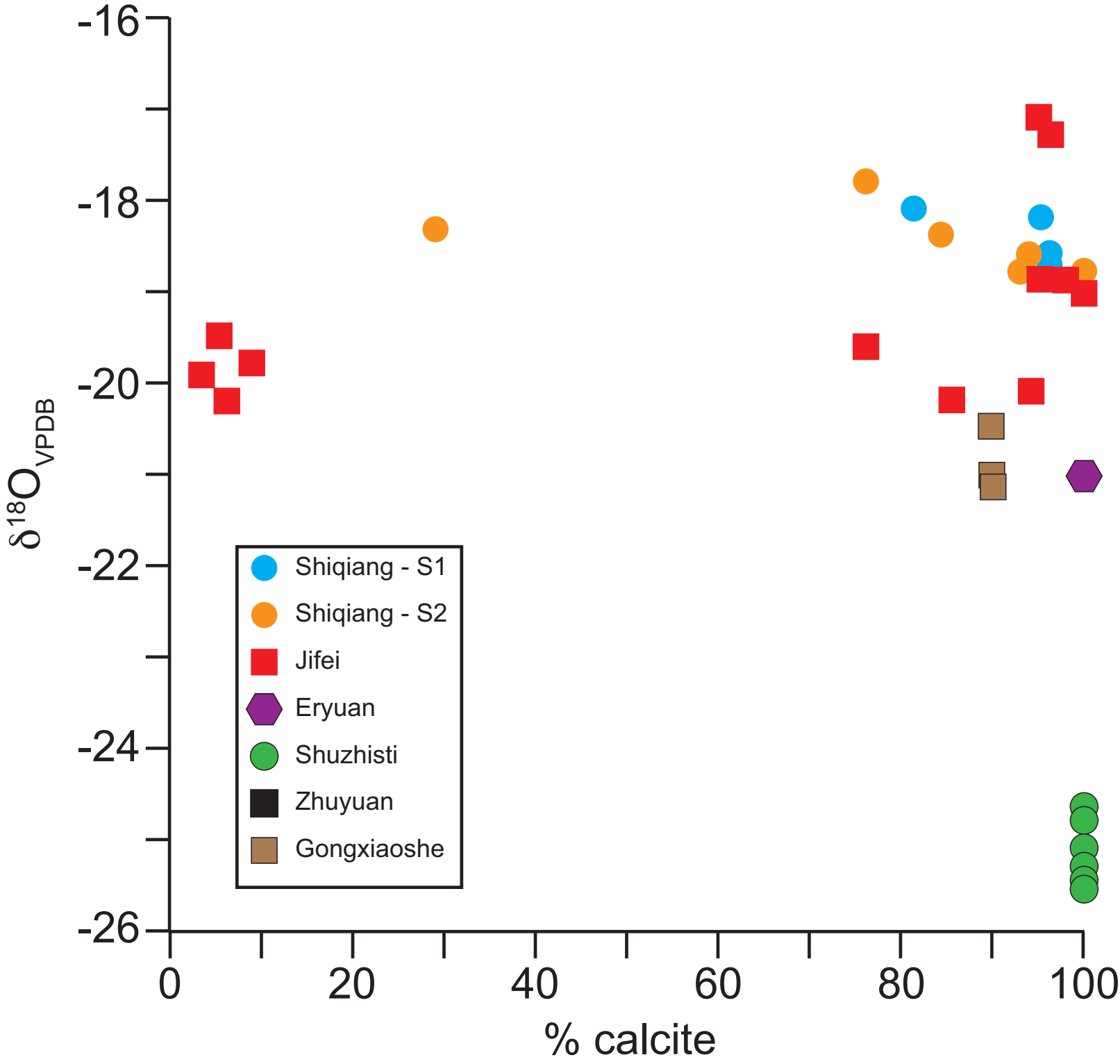
-16
-18
-20
-22
-24
-26
δ18OVPDB
0
20
40
60
80
100
% calcite
Shiqiang - S1
Shiqiang - S2
Jifei
Eryuan
Shuzhisti
Zhuyuan
Gongxiaoshe

Figure 17

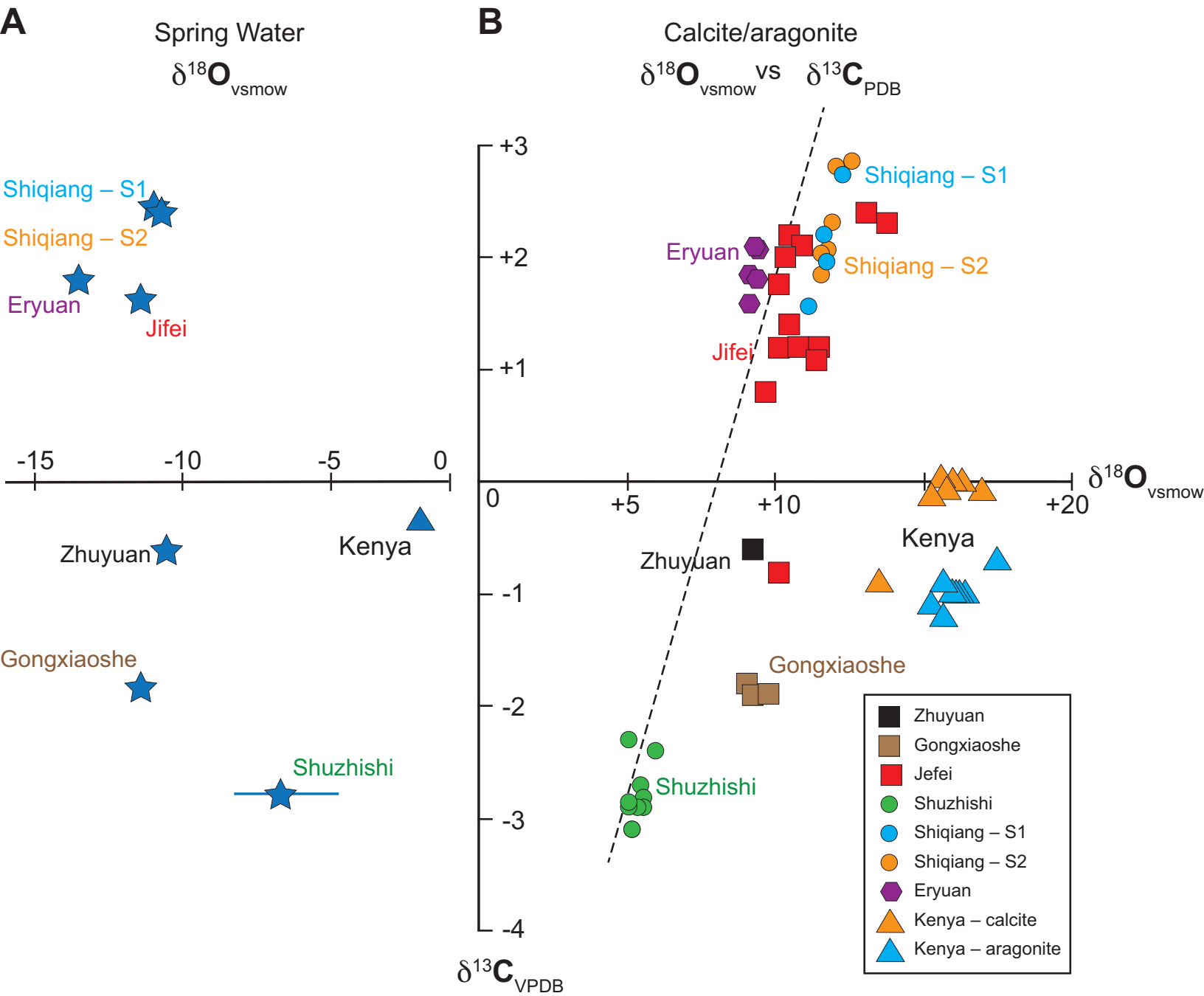
A
Spring Water
δ18Ovsmow
Shiqiang – S1
Shiqiang – S2
Eryuan
Jifei
-15
-10
-5
0
Zhuyuan
Kenya
Gongxiaoshe
Shuzhishi
B
Calcite/aragonite
δ18Ovsmow vs δ13CPDB
+3
+2
+1
-1
-2
-3
-4
0
+5
+10
+20
δ18Ovsmow
δ13CVPDB
Shiqiang – S1
Eryuan
Shiqiang – S2
Jifei
Zhuyuan
Kenya
Gongxiaoshe
Shuzhishi
Zhuyuan
Gongxiaoshe
Jefei
Shuzhishi
Shiqiang – S1
Shiqiang – S2
Eryuan
Kenya – calcite
Kenya – aragonite

Figure 18

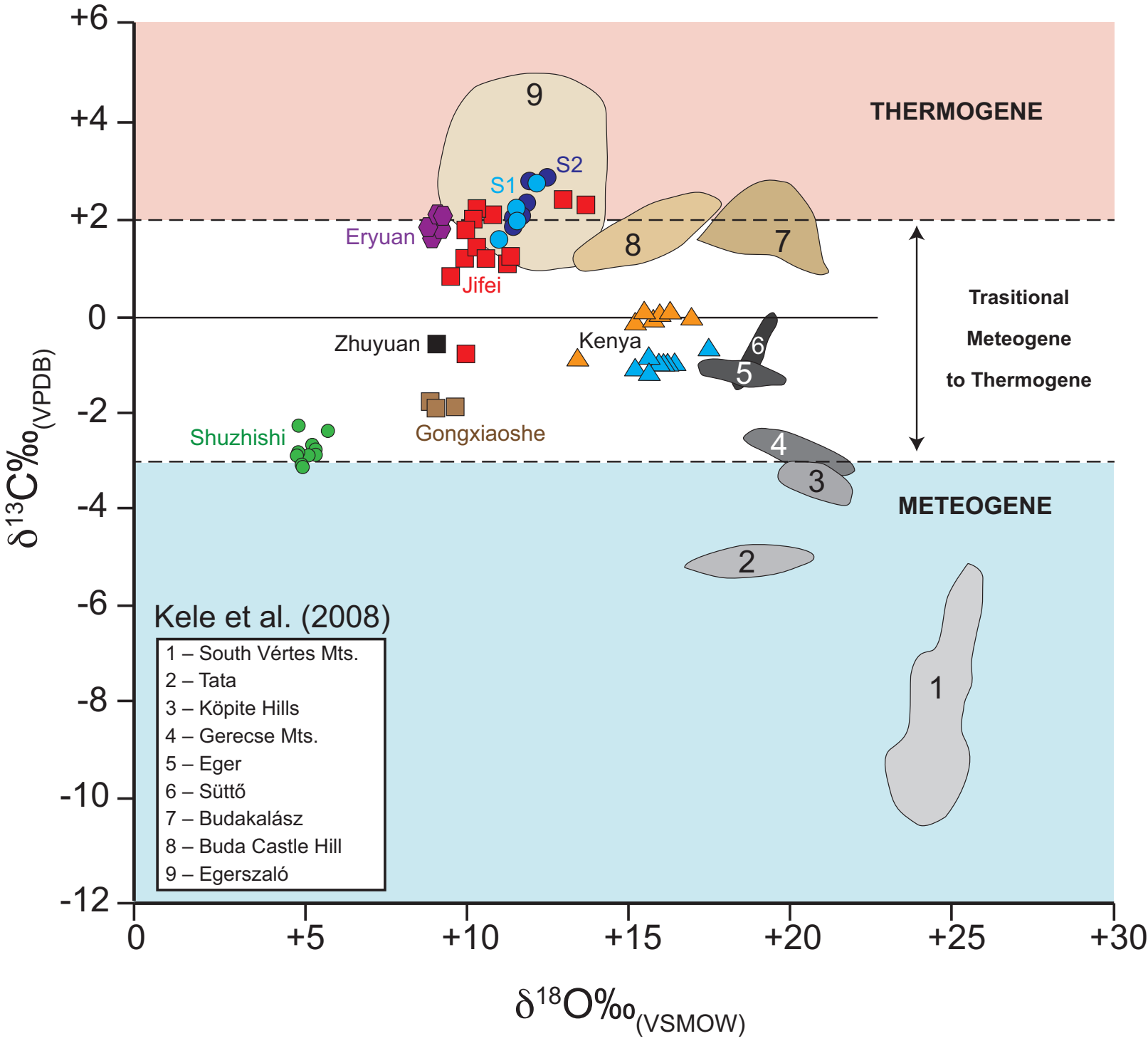
THERMOGENE
METEOGENE
Trasitional
Meteogene
to Thermogene
9
8
7
6
5
4
3
2
1
S1
S2
Eryuan
Jifei
Zhuyuan
Kenya
Gongxiaoshe
Shuzhishi
Kele et al. (2008)
1 – South Vértes Mts.
2 – Tata
3 – Köpite Hills
4 – Gerecse Mts.
5 – Eger
6 – Süttő
7 – Budakalász
8 – Buda Castle Hill
9 – Egerszaló
+6
+4
+2
0
-2
-4
-6
-8
-10
-12
0
+5
+10
+15
+20
+25
+30
δ13C‰(VPDB)
δ18O‰(VSMOW)

Table 1
Click here to download Table: Table 01 Water Comparisons.docx

Table 1. Chemical analyses of waters from hot springs located in Ruidian geothermal area. Given that Guo and Wang (2012) did not give exact locations for springs I and II at Shiqiang, it is not known if they are the same as the springs designated S1 and S2 in this paper.

Spring	T°C	pH (Field)	pH (Lab)	Na	K	Ca	Mg	HCO_3	Cl	SO_4	Fe	SiO_2
Shiqiang												
S1[1]	82.5	6.70	7.97	435	60	65	22	1510	62	0.2	0.01	46
S2[1]	56.6	6.77	8.02	450	64	69	24	1600	57	0.2	0.03	45
Spring I[2]	66.7	6.56	–	291	45	204	17	–	50	2	–	80
Spring II[2]	31.1	5.93	–	4	2	56	3	–	1	6	–	11
LaXin[3]												
Gongxiaoshe	74.9	8.5	–	165	43	5	6.3	939	200	34.5	–	180
Gongxiaoshe	73.5	7.5	8.2	421	44	21	3.8	983	164	28.0	–	139
Zhuyuan	82.1	6.8	7.8	390	43	25	4.0	938	154	27.0	–	128
Jifei[4]												
Female Tower Spring	79.0	6.6	7.9	170	57	58	13	702	13	9.3	–	74
Male Tower Spring	83.0	6.9	7.8	169	20	56	13	705	21	11.0	–	73
Big Steam Pool	65.3	7.7	7.8	169	20	58	13	705	13	11.0	–	74
Big Stone Pot Spring	62.3	6.9	9.0	171	20	58	13	714	17	11.0	–	74
Eryuan[5]	88.0	–	7.5	107	9	117	21	360	225	272.0	–	48

[1] This study. Concentrations in mg/L.
[2] From Guo and Wang (2012, their Tables 1 and 2). Concentrations in mg/L.
[3] From Jones and Peng (2014b, their Table 1). Concentrations in mg/L.
[4] From Jones and Peng (2014a, their Table 1). Concentrations in mg/L.
[5] From Jones and Peng (2012a, their Table 1). Concentrations in mg/L.

Table 2. Saturation indices calculated from water samples collected from springs at Shiqiang, Gongxiaoshe, Zhuyuan, Erjuan, and Jifei. Saturation levels calculated using PHREEQC Interactive (v 3.3.3) and Waterp4F Database (Parkhurst and Appelo, 1999).

	Shiqiang	Shiqiang	Gongxiaoshe		Zhuyuan	Eryuan	Jifei
Mineral	S1	S2	1	2			Big Steam Pool
Aragonite	-0.1	-0.1	0.45	0.70	0.21	1.29	1.17
Calcite	0.01	0.03	0.57	0.81	0.32	1.40	1.28
Dolomite	-1.25	-0.89	0.85	1.37	0.23	2.39	2.45
Goethite	2.77	3.52	—	—	—	—	—
Gypsum	-4.41	-4.48	-3.28	-2.83	-2.70	—	-2.75
Hematite	7.77	9.17	—	—	—	—	—
Quartz	-2.05	-2.14	-1.2	0.4	0.27	-0.22	0.21
SiO_2(a)	-3.00	-3.22	-2.19	-0.6	-0.68	-1.15	-0.83
Talc	14.87	15.24	16.05	3.94	0.41	5.82	5.16

Table 3
Click here to download Table: Table 3 percent calcite and isotopes.docx

Table **. $\delta^{18}O_{PDB}$ and $\delta^{13}C_{PDB}$ values for samples of $CaCO_3$ precipitates from various springs in Yunnan Province. The %calcite and %aragonite were determined from XRD analyses for all samples except for those from Gongxiaoshe and Zhuyuan that came from thin section analyses. The XRD analysis are ±10%. Data sources: Shiqiang – this paper; Shuzhisti – Jones and Peng (2012b, their Table 2), sample # is height above base of section; Jifei – data and sample numbers from Jones and Peng (2014a, their Table 4); Gongxiaoshe and Zhyuan from Jones and Peng (2014b, their Table 2)

Spring	Sample #	% calcite	% aragonite	$\delta^{18}O_{VPDB}$	$\delta^{13}C_{VPDB}$‰
Shiqiang – S1	1	96	4	-18.62	1.97
Shiqiang – S1	2	96	4	-18.70	2.21
Shiqiang – S1	3	95	5	-18.22	1.50
Shiqiang – S1	10	81	19	-18.08	2.74
Shiqiang – S2	4	76	24	-17.80	2.86
Shiqiang – S2	5	29	71	-18.33	2.81
Shiqiang – S2	6	94	6	-18.57	2.06
Shiqiang – S2	7	93	7	-18.76	2.04
Shiqiang – S2	8	100	0	-18.79	1.84
Shiqiang – S2	9	84	16	-18.43	2.30
Shuzhisti	0.60 m	100	0	-24.65	-2.65
Shuzhisti	0.61 m	100	0	-24.84	-2.89
Shuzhisti	1.95 m	100	0	-24.58	-2.79
Shuzhisti	2.00 m	100	0	-25.11	-3.11
Shuzhisti	3.00 m	100	0	-24.85	-2.87
Shuzhisti	3.02 m	100	0	-24.79	-2.92
Shuzhisti	3.05 m	100	0	-24.82	-2.86
Shuzhisti	3.10 m	100	0	-24.98	-2.97
Shuzhisti	5.00 m	100	0	-24.62	-2.87
Shuzhisti	5.02 m	100	0	-25.02	-3.12
Shuzhisti	6.00 m	100	0	-25.10	-2.94
Shuzhisti	6.02 m	100	0	-24.19	-2.40
Jifei	1A	3	97	-19.87	2.01

Jifei	1B	6	94	-20.24	1.76
Jifei	1C	85	15	-20.24	-0.80
Jifei	2A	76	24	-19.60	1.18
Jifei	3	100	0	-19.02	1.08
Jifei	4	6	94	-19.53	2.10
Jifei	5A	95	5	-16.60	2.28
Jifei	5B	95	5	-18.90	1.21
Jifei	2B	94	6	-20.09	1.15
Jifei	2(1)	96	4	-17.31	2.42
Jifei	2(2)	98	2	-19.82	1.39
Jifei	2(3)	9	91	-19.78	2.16
Gongxiaoshe*	A	90	10	-20.52	-1.74
Gongxiaoshe*	B	90	10	-21.04	-1.90
Gongxiaoshe*	C	90	10	-21.19	-1.92
Zhuyuan*	A	95	5	-20.98	-0.62
Eryuan	1	100	0	-21.41	1.85
Eryuan	2A	100	0	-21.11	2.07
Eryuan	2B	100	0	-21.03	1.81
Eryuan	4A	100	0	-21.40	2.08
Eryuan	4B	100	0	-21.37	1.59

Table 4
Click here to download Table: Table 04 13C of carrier CO2.docx

Table 4. Calculated $\delta^{13}C_{CO_2}$ ‰ (to first decimal place) from $\delta^{13}C_{CaCO_3}$ ‰based on equations and/or graphical relationships in Emrich et al. (1970), Panichi and Tongiorgi (1975) Chacko et al. (1991, 2001), and Romanek et al. (1992). $\delta^{13}C_{CaCO_3}$ values are average value derived from all samples analyzed for specified location; water T is for modern water. See text for further discussion.

Locality	$\delta^{13}C_{CaCO_3}$	Water T (°C)	Calculated $\delta^{13}C_{CO_2}$ ‰ for carrier CO_2			
			Emrich et al. (1970)[1]	Panichi & Tongiorgi (1976)[2]	Chacko et al. (1991, 2001)	Romanek et al. (1992)
Shiqiang –S1	2.11	82.5	-4.6	-8.0	-3.1	0.0
Shiqiang – S2	2.14	56.6	-6.0	-7.9	-5.2	-3.1
Jifei	1.49	83.0	-5.5	-8.7	-3.6	-0.5
Eryuan	1.88	88.0	-4.5	-8.2	-2.9	0.5
Gongxiaoshe	-1.85	75.0	-9.0	-12.7	-7.6	-4.8
Zhuyuan	-0.62	82.0	-7.3	-11.2	-5.8	-2.8
Shuzhisti	-2.86	80.0	-9.9	-13.9	-8.2	-9.9

[1] Based on extrapolation of graphical plot (line b) in Figure 1 of Emrich et al. (1970)

[2] Calculated using equation $\delta^{13}C_{CO2} = (1.2(\delta^{13}C_{CaCO_3}) - 10.5)$ as specified by Panichi and Tongiorgi (1976)

[3] Based on equation from Chacko et al. (2001)

[4] Based on fractionation factor (11.98-(0.12*T°C) as specified by Romanek et al. (1992).

Table 5
Click here to download Table: Table 05- Spring comparisons.docx

Table 3. Comparison of calcite deposits at various springs in Yunnan Province. ACC = amorphous calcium carbonate.

Feature	Spring						
	Shiqiang		Ruidian		Eryuan	Jifei	Shuzhishi
	S1	S2	Gongxiaoshe	Zhuyuan			
	(This paper)		(Jones & Peng, 2014b)		(Jones & Peng, 2012a)	Jones & Peng, 2014a)	(Jones & Peng, 2012b)
Setting	Pool	Pool	Pool	Pool	Pool	Outflow	Inactive
Water T (°C)	82.5	56.6	74.9	82.1	88.0	79.0	–
Water pH	6.7	6.8	8.5	6.8	7.5	7.0	–
Calcite	Yes	Yes	Yes	Yes	Yes	Yes	Yes
ACC	No	No	Yes	Yes	Yes	No	No
Aragonite	Yes	Yes	Yes	Yes	Yes	Yes	No
Calcite alteration	No	No	No	No	No	No	Yes
Aragonite alteration	No	No	No	No	No	Yes	–
Calcite overgrowths	Yes	Yes	No	No	No	No	Yes
Loose dodecahedra	Yes	Yes	Yes	Yes	Yes	Yes	No
Loose rhombohedra	Yes	Yes	Yes	Yes	Yes	Yes	No
Microbes	Yes	Yes	Yes	Yes	Yes	Yes	Yes
Opal	Opal-A	Opal-A	No	No	Opal-A	Opal-A	Opal-CT
Si-Mg reticulate coatings	No	No	Yes	Yes	No	Yes	Yes
Accessory minerals	–	–	–	Gypsum Barite	–	Trona Barite K-sulfate Mirabillite Gaylussite	Mn-precipitates